World Scientific
www.worldscientific.com

Locking-Free Kriging-Based Curved Beam Elements with the Discrete Strain Gap Technique

F. T. Wong [ID]*

Department of Civil Engineering, Petra Christian University
Jl. Siwalankerto 121-131, Surabaya 60236, Indonesia
wftjong@petra.ac.id

Junius Gunawan [ID]

Postgraduate Program in Civil Engineering
Faculty of Civil Engineering and Planning
Petra Christian University, Jl. Siwalankerto 121-131
Surabaya 60236, Indonesia
juniusgunawan999@gmail.com

Kriging-based finite element method (K-FEM) is an enhancement of the FEM using Kriging interpolation in place of the conventional polynomial interpolation. This paper presents the development of the K-FEM for analysis of curved beams based on a deep arc theory, which accounts for membrane and shear deformation. The discrete strain gap technique is employed to circumvent shear locking and membrane locking. The numerical tests show that the Kriging-based elements are free from any locking, are able to provide highly accurate solutions with a regular course mesh discretization, and have excellent convergence characteristics, especially for circular beams.

Keywords: Curved beam; Kriging-based finite element; shear locking; membrane locking; discrete strain gap.

1. Introduction

1.1. *Curved beam elements, shear locking, and membrane locking*

Curved beam elements have been the subject of much research since the early development of the finite element method (FEM). The motivations for this research are: (a) curved beams, particularly circular-shaped arcs, are quite useful in structural engineering practice, (b) a reliable, high-performance curved beam element is difficult to develop because of the difficulties of stretching-flexural interaction,

---

*Corresponding author.

F. T. Wong & J. Gunawan

Table 1. References related to FEMs for different curved beam models.

Curved beam theory	Examples of references related to FEMs
Deep arch theory	Babu and Prathap [1986], Prathap and Babu [1986], Saleeb and Chang [1987], Day and Potts [1990], Zhang [1992], Lee and Sin [1994], Prathap [1994], Ryu and Sin [1996], Kim and Kim [1998], Raveendranath *et al.* [1999; 2001], Kim and Park [2006; 2008], Echter and Bischoff [2010], Shahba *et al.* [2013], Bouclier *et al.* [2012] and Yang *et al.* [2014]
Shallow arch theory	Stolarski and Belytschko [1982; 1983] and Koschnick *et al.* [2005]
Degenerated-solid beam	Prathap and Naganarayana [1990], Koziey and Mirza [1994], Nascimbene [2013] and Wei *et al.* [2022]

Note: This table is not intended to be a comprehensive literature on the FEM for curved beam models. It only includes the most relevant works for this study.

rigid-body mode representation, and shear-membrane locking phenomena [Babu and Prathap (1986); Kim and Park (2006); Lee and Sin (1994); Ryu and Sin (1996); Saleeb and Chang (1987)], and (c) the study of curved beam elements gives an insight into the more complex behavior of shell elements [Cook *et al.* (2002); Kim and Park (2006, 2008); Lee and Sin (1994); Nascimbene (2013); Saleeb and Chang (1987)].

There are three approaches to modeling curved beams: (1) a deep arc (or deep shell) theory with a curvilinear coordinate, (2) a shallow arch (or shallow shell) theory, and (3) the degenerated-solid (or continuum-based) beam approach. Relevant references for each approach are listed in Table 1. In developing curved beam elements, regardless of which approach is adopted, difficulties with shear locking and membrane locking may be present. The shear locking phenomenon is a condition where the beam finite element model becomes excessively stiff as the beam thins out due to the magnification of the shear strain energy error. Membrane locking is a condition where the beam finite element model becomes excessively stiff as the beam increasingly thins or the curvature becomes increasingly large, due to the magnification of the membrane (or axial) strain energy error. The root cause of shear locking is an inconsistency in the approximation of shear strain so that the resulting finite element model is unable to represent pure bending deformation without producing shear strain (shearless bending). Likewise, membrane locking results from an inconsistency in the approximation of membrane strain so that the resulting finite element model is unable to represent pure bending deformation without stretching (inextensional bending).

Various concepts, techniques, or tricks have been introduced to overcome shear locking and membrane locking. One of the earliest techniques is the selective reduced integration (SRI) technique, which has been applied to straight Timoshenko beams [Hughes *et al.* (1977)] and then to curved beams [Day and Potts (1990); Stolarski and Belytschko (1982, 1983); Zhang (1992)]. Prathap and Babu [1986] introduced least-squares smoothed shape functions to achieve consistency in the shear strain

and membrane strain approximated fields. An alternative way to achieve consistency is to expand the 'troublesome' constrained shear strains in terms of the Legendre polynomial and then drop the inconsistent terms [Prathap (1994); Prathap and Naganarayana (1990)].

Several curved beam elements based on the Hellinger–Reissner variational principle, using field-consistent approximations for the stress resultants, have been shown to be free from shear and membrane locking [Kim and Kim (1998); Kim and Park (2006, 2008); Saleeb and Chang (1987); Zhang (1992)]. In the context of degenerated-solid beam elements, a consistent formulation has been achieved by providing a cubic polynomial for the tangential and radial displacement fields and a quadratic polynomial for the rotation field [Koziey and Mirza (1994)].

Several strain-based elements, employing either the whole strain field approximations [Choi and Lim (1995)] or partial strain approximations [Lee and Sin (1994); Ryu and Sin (1996)], have been proposed to avoid locking difficulties. The strain–displacement relations or homogeneous equilibrium equations were used to relate the strain parameters and the nodal displacement components. These elements are free from locking and show remarkable accuracy in a relatively coarse mesh discretization.

Shahba *et al.* [2013] presented a set of shape functions derived through a step-by-step flexibility-based procedure. The shape functions automatically circumvent the difficulties of shear locking and membrane locking. Although the flexibility-based shape functions work well for arbitrary curved nonprismatic beams, the procedure is unlikely to be applied to general shell problems.

In the framework of meshfree methods (see e.g., [Liu (2016)] for an overview of meshfree methods), Wang and Chen [2006] presented a locking-free curved beam meshfree method using a moving least squares/reproducing kernel approximation (MLS/RK) as the trial function. To prevent membrane locking and shear locking, the MLS/RK approximation was constructed with the ability to represent pure bending deformation without producing parasitic shear and membrane strains. In addition, a nodal integration was developed to fulfill the bending exactness and integration constraints, as well as to remove the rank deficiency in the nodal integration of the Galerkin weak form.

Bletzinger *et al.* [2000] presented a unified approach, called the discrete shear gap (DSG) technique, to eliminate shear locking in shear deformable beams, plates, and shells. In this technique, the displacement-based shear strains are replaced with substitute shear strains determined from the interpolated shear gaps. The key advantage of the DSG technique is that it is applicable to shear-deformable triangular or rectangular plate elements of any polynomial degree [Bletzinger *et al.* (2000)], without any additional artifices, such as a particular choice of sampling point or the introduction of a bubble shape function. Subsequently, [Koschnick *et al.* (2005)] extended this DSG technique to a more general concept and renamed

'DSG' as the 'discrete *strain* gap'. The same concept as the DSG technique was used to eliminate the membrane locking in curved finite elements of the beam and shell.

Applications and numerical tests of the DSG technique presented in the original papers [(Bletzinger *et al.* (2000); Koschnick *et al.* (2005)] were focused on the plate and shell problems. In the framework of NURBS (NonUniform Rational B-Splines) finite element [Cottrell *et al.* (2009); Hughes *et al.* (2005)], the DSG technique has been successfully applied to eliminate shear locking in the Timoshenko beam model [Echter and Bischoff (2010)] and to eliminate both shear locking and membrane locking in the curved shear-deformable beam model [Bouclier *et al.* (2012)]. Wong and Sugianto [2017] applied the DSG technique to the conventional Timoshenko beam elements of different polynomial bases. The results showed that the DSG works very well for all elements of different degrees, to eliminate the shear locking and give correct shear force distributions. However, the DSG technique has not been formulated and tested for curved beam models that are discretized using an enhanced FEM with Kriging interpolation (KI) [Wong and Kanok-Nukulchai (2009a)]. Therefore, this paper aims to present applications of the DSG technique to so-called Kriging-based shear-deformable curve beam elements. The enhanced FEM with KI is reviewed in the following sub-section.

1.2. *Kriging-based FEM*

Kriging is a well-known geostatistical technique for spatial data interpolation [Olea (2018); Wackernagel (2003)]. The basic idea of Kriging is that any unknown value at a point can be estimated from a linear combination of known values at the points in its specified neighborhood. Originating from a type of meshfree method, that is, the element-free Galerkin method with moving KI [Gu (2003); Plengkhom and Kanok-Nukulchai (2005)] presented an enhancement of the FEM by adopting KI as the trial function, in place of the traditional polynomial interpolation. Using the KI, the shape functions can be freely generated over any finite set of nodes, which include the element nodes as well as the surrounding nodes outside the element (called satellite nodes). The element nodes and satellite nodes constitute a domain of influencing nodes (DOI), which may extend over several layers of elements. This enhanced FEM was subsequently called 'Kriging-based FEM' (K-FEM) [Wong and Kanok-Nukulchai (2009a)].

The K-FEM has several advantages [Kanok-Nukulchai *et al.* (2015); Wong and Kanok-Nukulchai (2009b)]. First, highly accurate solutions can be obtained even by using a mesh of the simplest form of elements (triangles in a 2D domain or tetrahedrons in a 3D domain). Second, solution improvement can be achieved without additional element nodes or degrees of freedom. This is because the K-FEM accuracy can be enhanced by including a higher degree basis function in the KI (other than a linear basis) or by enlarging the element-layered DOI. Lastly, the K-FEM

can also be easily incorporated into existing general-purpose FE codes because the K-FEM computational procedure is very similar to the standard FEM.

A drawback of the K-FEM is that it is computationally more expensive than the standard FEM. The reasons for this are: (a) there are no explicit expressions for the Kriging shape functions; they are constructed for each element during the computer running process. (b) A larger DOI produces larger element stiffness matrices and a larger bandwidth of the global stiffness matrix. Another disadvantage of the K-FEM is that it faces difficulty in the application to models that have gradient continuities, such as a solid body made from different materials [Sommanawat (2010)] and a beam subjected to some concentrated forces (see the example of Sec. 5.4), so it requires special treatment to handle the discontinuities.

As in the standard FEM, in the applications of the K-FEM to shear-deformable beams, plates, and shells, the difficulties of shear locking and membrane locking are also present. The use of a sufficiently high degree polynomial basis (i.e., a cubic or quartic basis) embedded in the KI has been used in the previous works on Reissner–Mindlin plates [Wong and Kanok-Nukulchai (2006, 2009a)] and degenerated-3D-solid shells [Wong *et al.* (2015)], to alleviate the locking phenomena. This exercise, however, can only *alleviate* but cannot *eliminate* the locking phenomena. Moreover, it makes the computational cost high because it requires a DOI covering three or four layers of elements. Therefore, a more effective and efficient technique to eliminate the locking in the K-FEM for plates and shells is desirable.

To gain insight into a technique for the elimination of locking, the application of the SRI and DSG techniques has been examined in the K-FEM for straight Timoshenko beams (K-beam elements) [Wong *et al.* (2018, 2022, 2024); Wong and Syamsoeyadi (2011)]. As in conventional FEM, the SRI technique is effective at eliminating shear locking in the K-beam elements [Wong and Syamsoeyadi (2011)]. However, the use of this technique yields oscillatory, incorrect shear force distribution along the beam. The DSG technique with a modified implementation also works well to eliminate the shear locking in the K-beam elements [Wong *et al.* (2022, 2024)]. The elements can produce very accurate results for the deflection, rotation, and bending moment. The resulting shear force distribution, however, is piecewise constant, as in the conventional linear Timoshenko beam element with the DSG [Wong and Sugianto (2017)].

In this paper, we developed a family of Kriging-based finite elements for the linear static analysis of curved beams. The curved beam elements are developed based on a deep arc theory, with the strain definitions given by Day and Potts [1990]. The DSG technique [Bletzinger *et al.* (2000); Koschnick *et al.* (2005)] is employed to eliminate both shear locking and membrane locking. A series of numerical tests are then carried out to show the elements' performance concerning their locking-free property, accuracy, and convergence. The resulting Kriging-based curved beam elements can be regarded as a further development of the straight Kriging-based Timoshenko beam elements with the DSG technique [Wong *et al.* (2022, 2024)].
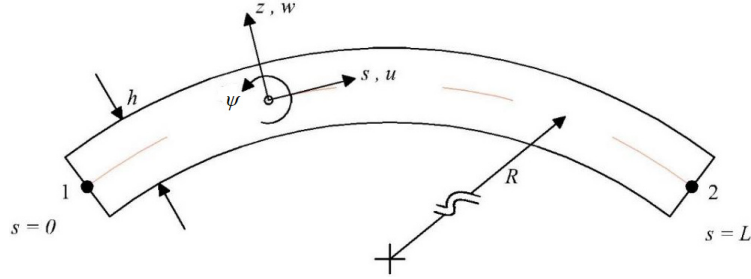
F. T. Wong & J. Gunawan

Fig. 1. Curved beam segment of the arch length L, radius of curvature R, and thickness h.

The novelties of this study are, first, it presents the development of an *isoparametric* K-FEM. Although the isoparametric concept is a standard approach in the formulation of conventional FEMs, it has not been utilized in previous works on K-FEMs. Second, this study applies the DSG technique to eliminate membrane locking in the frameworks of K-FEM.

2. Governing Equations of Shear-Deformable Curved Beam Elements

We consider a curve beam segment of the radius of curvature R, arc length L, and thickness h, where $h \ll R$, as illustrated in Fig. 1. A coordinate system $s - z$ is defined along the mid-curve, where the s-axis is the curvilinear abscissa in the circumferential (or tangential) direction and the z-axis is the ordinate following the local outward radial direction. A point on the mid-curve has a tangential displacement component u (in the s-direction) and radial displacement component w (in the z-direction). The motion of the beam can be described in terms of the tangential displacement field $u = u(s)$, radial displacement field $w = w(s)$, and cross-sectional rotation field $\psi = \psi(s)$ [Cook *et al.* (2002)].

The relations between the displacement components and the membrane strain ε_m, curvature κ, and shear strain γ_{sz} are given as [Day and Potts (1990)]

$$\varepsilon_m = u_{,s} + \frac{w}{R}, \tag{1a}$$

$$\kappa = -\psi_{,s}, \tag{1b}$$

$$\gamma_{sz} = w_{,s} - \psi - \frac{u}{R}, \tag{1c}$$

where commas followed by s ($_{,s}$) after the quantities u, ψ, and w stand for the derivative of the quantities with respect to variable s.

The membrane (or axial) force N, bending moment M, and shear force V are related to the generalized strains as follows:

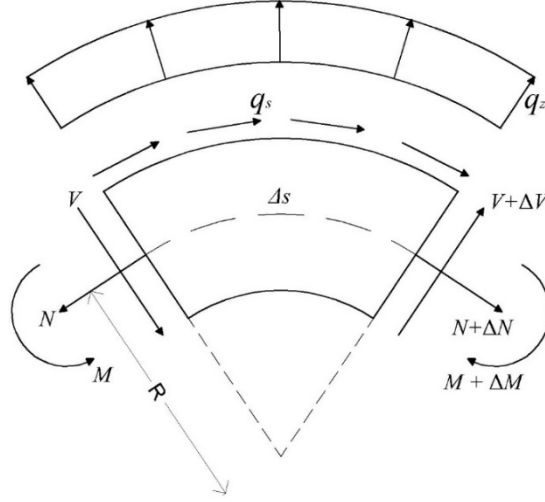$$N = EA\varepsilon_m, \tag{2a}$$

$$M = EI\kappa, \tag{2b}$$

Fig. 2. Free-body diagram of an infinitesimal curved beam segment.

$$V = GA_{\mathrm{s}}\gamma_{sz}, \tag{2c}$$

where E is the modulus of elasticity, A is the cross-sectional area, I is the moment of inertia, G is the shear modulus, and $A_s = kA$ is the effective shear area, in which k is the shear correction factor [Cowper (1966)]. The positive sign convention for these stress resultants is shown in Fig. 2.

The equilibrium equations of an infinitesimal curved beam segment, as shown in Fig. 2, can be written as [Oden (1967)]

$$\frac{dN}{ds} + \frac{V}{R} + q_{\mathrm{s}} = 0, \tag{3a}$$

$$\frac{dV}{ds} - \frac{N}{R} + q_{\mathrm{z}} = 0, \tag{3b}$$

$$\frac{dM}{ds} - V - m = 0, \tag{3c}$$

where q_s, q_z, and m are the external loads, i.e., the distributed tangential force, distributed radial force, and distributed moment (not shown in Fig. 2; the positive sign follows the cross-sectional rotation ψ), respectively.

The weak form of the governing equations for the curved beam segment can be obtained using the principle of virtual displacements, i.e.,

$$\int_0^L \delta\varepsilon_m EA\varepsilon_m ds + \int_0^L \delta\kappa EI\kappa ds + \int_0^L \delta\gamma_{sz} GA_{\mathrm{s}}\gamma_{sz} ds = \int_0^L \delta\mathbf{u}^T \mathbf{f} ds + \delta\mathbf{U}^T \mathbf{F}$$

$$\forall\, \delta u, \delta w, \delta\psi \in V = \{v | v \in \mathrm{H}^1(0, L)\}, \tag{4a}$$

$$\delta\mathbf{u} = [\delta u \quad \delta w \quad \delta\psi]^T, \tag{4b}$$
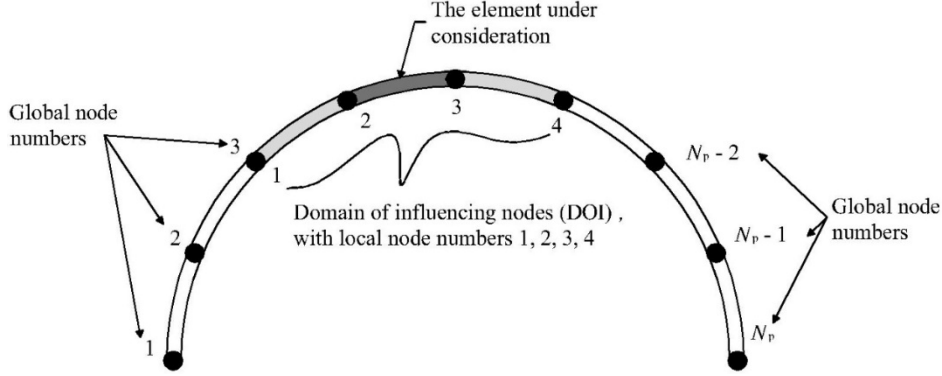
F. T. Wong & J. Gunawan

Fig. 3. Curve beam structure with N_p global nodes and an example of the two-layer DOI for the element under consideration.

$$\mathbf{f} = [q_s \quad q_z \quad m]^T, \tag{4c}$$

$$\delta\mathbf{U} = [\delta u_1 \quad \delta w_1 \quad \delta\psi_1 \quad \delta u_2 \quad \delta w_2 \quad \delta\psi_2]^T, \tag{4d}$$

$$\mathbf{F} = [F_{s1} \quad F_{z1} \quad M_1 \quad F_{s2} \quad F_{z2} \quad M_2]^T. \tag{4e}$$

The left-hand side of Eq. (4a) is the virtual strain energy of the curved beam segment, which consists of three parts, i.e., the virtual membrane strain energy, the virtual bending strain energy, and the virtual shear strain energy. Symbols δu, δw, and $\delta\psi$ are a virtual circumferential displacement field, a virtual radial displacement field, and a virtual cross-sectional rotation field, respectively. Space $H^1(0, L)$ is the Sobolev function space of the first degree in interval $0 < s < L$. Vector $\delta\mathbf{U}$ lists the virtual displacement components at the two ends of the element (that is, at $s = 0$ and $s = L$). Corresponding to $\delta\mathbf{U}$, vector $\mathbf{F}$ lists the equilibrating forces and moments at the two ends of the curved beam.

3. Kriging-Based Curved Beam Element Formulation

Suppose a curved beam structure is subdivided into N_e two-node elements with the total number of nodes N_p. We consider a typical curved beam element (element number e) with a predefined DOI extending over two or three layers of elements, covering n nodes inside and outside the element, as illustrated in Fig. 3 for the case of two-layer DOI.

The field variables over the element are approximated using KI over the DOI, including the element nodes and the satellite nodes, as follows:

$$u \cong u^h = \sum_{i=1}^{n} \lambda_i u_i = \mathbf{\Lambda}_u \mathbf{d^e}, \tag{5a}$$

$$w \cong w^h = \sum_{i=1}^{n} \lambda_i w_i = \boldsymbol{\Lambda}_w \mathbf{d^e}, \tag{5b}$$

$$\psi \cong \psi^h = \sum_{i=1}^{n} \lambda_i \psi_i = \boldsymbol{\Lambda}_\psi \mathbf{d^e}. \tag{5c}$$

In these equations, superscript h indicates that the corresponding field variable is approximated using a characteristic finite element size h. Vector $\mathbf{d}^e$ is the vector of displacement values at all nodes in the DOI of element e (that is, including the element nodes and the satellite nodes), which is defined as

$$\mathbf{d^e} = \left\{ u_1 \quad w_1 \quad \psi_1 \quad u_2 \quad w_2 \quad \psi_2 \quad \dots \quad u_n \quad w_n \quad \psi_n \right\}^{\mathrm{T}}. \tag{6}$$

Matrices Λ_u, Λ_w, and Λ_ψ are the shape function matrices for the circumferential displacement, the radial displacement, and the rotation, respectively, viz.

$$\boldsymbol{\Lambda}_u = \begin{bmatrix} \lambda_1 & 0 & 0 & \lambda_2 & 0 & 0 & \dots & \lambda_n & 0 & 0 \end{bmatrix}, \tag{7a}$$

$$\boldsymbol{\Lambda}_w = \begin{bmatrix} 0 & \lambda_1 & 0 & 0 & \lambda_2 & 0 & \dots & 0 & \lambda_n & 0 \end{bmatrix}, \tag{7b}$$

$$\boldsymbol{\Lambda}_\psi = \begin{bmatrix} 0 & 0 & \lambda_1 & 0 & 0 & \lambda_2 & \dots & 0 & 0 & \lambda_n \end{bmatrix}. \tag{7c}$$

The shape functions, $\lambda_i = \lambda_i(\xi)$, $i = 1, \dots, n$, are Kriging weights, which are parameterized using the natural coordinate ξ.

The relationship between the curvilinear coordinate s and the natural coordinate ξ is defined by a Kriging-based isoparametric mapping from a reference DOI to the physical DOI, i.e.,

$$s = \sum_{i=1}^{n} \lambda_i(\xi) s_i. \tag{8}$$

Here, the reference DOI covers the usual reference element and its surrounding elements, as illustrated in Fig. 4 for the case of a two-layer DOI.

The Kriging weights, $\lambda_i = \lambda_i(\xi)$, $i = 1, \dots, n$, are obtained by solving a system of universal Kriging normal equations, given as [Gu (2003); Olea (2018); Plengkhom and Kanok-Nukulchai (2005); Wackernagel (2003); Wong and Kanok-Nukulchai (2009a,b); Wong *et al.* (2018)]

$$\mathbf{R}\lambda(\xi) + \mathbf{P}\mu(\xi) = \mathbf{r}(\xi), \tag{9a}$$

$$\mathbf{P}^{\mathrm{T}}\boldsymbol{\lambda}(\xi) = \mathbf{p}(\xi), \tag{9b}$$

where

$$\mathbf{R} = \begin{bmatrix} C(h_{11}) & \dots & C(h_{1n}) \\ \dots & \dots & \dots \\ C(h_{n1}) & \dots & C(h_{nn}) \end{bmatrix}, \quad \mathbf{P} = \begin{bmatrix} p_1(\xi_1) & \dots & p_m(\xi_1) \\ \dots & \dots & \dots \\ p_1(\xi_n) & \dots & p_m(\xi_n) \end{bmatrix}, \tag{9c}$$

$$\boldsymbol{\lambda}(\xi) = \begin{bmatrix} \lambda_1(\xi) & \dots & \lambda_n(\xi) \end{bmatrix}^{\mathrm{T}}, \quad \boldsymbol{\mu}(\xi) = \begin{bmatrix} \mu_1(\xi) & \dots & \mu_m(\xi) \end{bmatrix}^{\mathrm{T}}, \tag{9d}$$
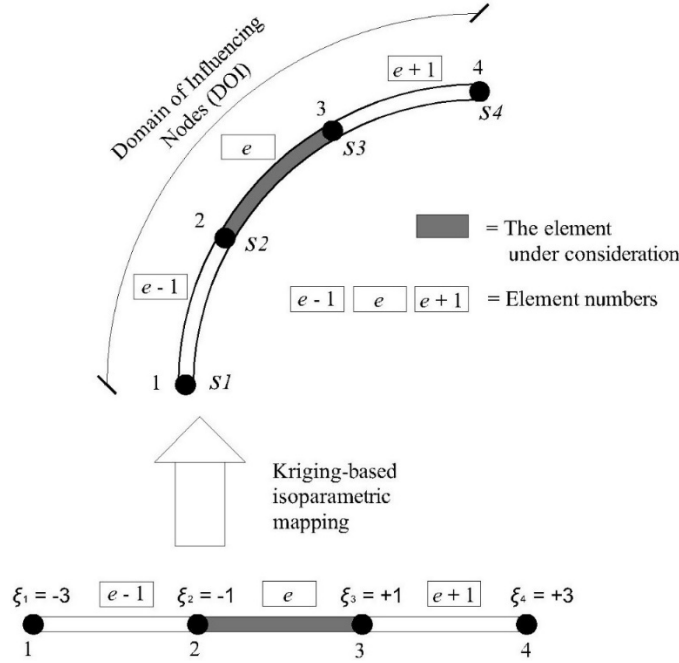
F. T. Wong & J. Gunawan

Fig. 4. Kriging-based mapping from the reference DOI to the physical DOI for a two-layer DOI.

$$\mathbf{r}(\xi) = [C(h_{1\xi}) \quad C(h_{2\xi}) \quad \ldots \quad C(h_{n\xi})]^{\mathrm{T}}, \tag{9e}$$

$$\mathbf{p}(\xi) = [p_1(\xi) \quad p_2(\xi) \quad \ldots \quad p_m(\xi)]^{\mathrm{T}}. \tag{9f}$$

In these equations, the unknown vectors are the $n \times 1$ vector of Kriging weights, $\lambda(\xi)$, and the $m \times 1$ vector of Lagrange multipliers, $\mu(\xi)$, where n is the number of nodes in the DOI and m is the number of polynomial basis functions. The given matrices and vectors are the $n \times n$ covariance matrix, $\mathbf{R}$, the $n \times m$ matrix of polynomial values at the nodes, $\mathbf{P}$, the $n \times 1$ vector of covariance, $\mathbf{r}(\xi)$, and the $m \times 1$ vector of polynomial basis, $\mathbf{p}$ (ξ). The covariance matrix $\mathbf{R}$ contains the covariance values between two random variables at two nodes with separating distances $h_{ij} = \xi_j - \xi_i$, $i, j = 1, \ldots, n$. The covariance vector $\mathbf{r}(\xi)$ contains the covariance values between random variables at the nodes in the DOI and random variable at the node of interest, ξ, with separating distances $h_{i\xi} = \xi - \xi_i$. A necessary condition to make the Kriging equation system solvable is that $n \geq m$.

To construct the Kriging shape functions or, in other words, to determine the Kriging weights, we need to decide the polynomial basis function and the covariance function. In this research, the polynomial basis functions used are linear, quadratic, and cubic basis functions, which have been used in previous research on Kriging-based finite elements for the analysis of Timoshenko beams [Wong *et al.* (2018, 2022, 2024)]. Once a polynomial basis has been selected, the size of the DOI, that is, the

number of element layers, must be chosen in such a way that it covers some nodes, n, that is greater than or equal to the number of polynomial bases, m. The minimum number of element layers for different polynomial bases has been presented in Wong *et al.* [2018]. It is worth noting that if a linear basis and one element-layer DOI are used, the resulting Kriging shape functions reduce to the standard linear shape functions.

The covariance function is more conveniently expressed in terms of the correlation function, i.e.,

$$\rho(h) = \frac{C(h)}{\sigma^2}, \tag{10}$$

where h is the distance between two points in the DOI and σ^2 is the variance of the random variable underlying the Kriging formulation [Wong and Kanok-Nukulchai (2009b); Wong *et al.* (2018)]. The correlation functions used are the Gaussian or quartic spline (QS) correlation models, i.e.,

$$\rho(h) = \exp\left(-\left(\theta_r \frac{h}{d}\right)^2\right), \tag{11a}$$

$$\rho(h) = \begin{cases} 1 - 6\left(\theta_r \dfrac{h}{d}\right)^2 + 8\left(\theta_r \dfrac{h}{d}\right)^3 - 3\left(\theta_r \dfrac{h}{d}\right)^4 & \text{for } 0 \le \theta_r \dfrac{h}{d} \le 1, \\ 0 & \text{for } \theta_r \dfrac{h}{d} > 1, \end{cases} \tag{11b}$$

where θ_r is a correlation parameter and d is the largest distance between two nodes in the DOI. A more detailed elaboration regarding appropriate ranges for the correlation parameters is presented in Wong *et al.* [2018].

To formulate the K-FEM, the integrals over the whole structure in the global weak form are written as the sum of integrals over all of the elements, that is,

$$\sum_{e=1}^{N_e} \int_0^{L^e} \delta\varepsilon_m EA\varepsilon_m ds + \sum_{e=1}^{N_e} \int_0^{L^e} \delta\kappa EI\kappa ds + \sum_{e=1}^{N_e} \int_0^{L^e} \delta\gamma_{sz} GA_s \gamma_{sz} ds$$

$$= \sum_{e=1}^{N_e} \int_0^{L^e} \delta\mathbf{u}^{\mathrm{T}} \mathbf{f} ds + \delta\mathbf{U}^{\mathrm{T}} \mathbf{F} \quad \forall \, \delta u, \delta w, \delta\psi \in \mathbb{V} = \{v \,|\, v \in \mathrm{H}^1(\Omega)\}, \tag{12}$$

where L^e is the arch length of element number e, $e = 1, 2, \ldots, N_e$. Inserting the Kriging approximated field variables, Eqs. (5a)–(5c), into Eq. (12) and applying the standard finite element formulation give the discretized matrix equation

$$\mathbf{KD} = \mathbf{F}_a + \mathbf{F}_{q_s} + \mathbf{F}_{q_z} + \mathbf{F}_m, \tag{13}$$

where $\mathbf{K}$ is the $3N_p \times 3N_p$ global structural stiffness matrix, $\mathbf{D}$ is the $3N_p \times 1$ structural nodal displacement vector, i.e.,

$$\mathbf{D} = [u_1 \quad w_1 \quad \psi_1 \quad u_2 \quad w_2 \quad \psi_2 \quad \cdots \quad \square \quad u_{N_p} \quad w_{N_p} \quad \psi_{N_p}]^{\mathrm{T}}, \tag{14}$$

$\mathbf{F}_a$ is the $3N_p \times 1$ vector of externally applied forces at the nodes, $\mathbf{F}_{qs}$, $\mathbf{F}_{qz}$, and $\mathbf{F}_m$ are the $3N_p \times 1$ vectors of equivalent nodal forces due to the distributed tangential

force q_s, due to the distributed radial force q_z, and due to the distributed moment m, respectively.

The global structural stiffness matrix is given as

$$\mathbf{K} = A_{e=1}^{N_e}\mathbf{k}_m^e + A_{e=1}^{N_e}\mathbf{k}_b^e + A_{e=1}^{N_e}\mathbf{k}_s^e, \tag{15a}$$

$$\mathbf{k}_m^e = \int_{-1}^{1} \mathbf{B}_m^{e^T} EA\mathbf{B}_m^{\mathbf{e}} Jd\xi, \tag{15b}$$

$$\mathbf{k}_b^e = \int_{-1}^{1} \mathbf{B}_b^{e^T} EI\mathbf{B}_b^e Jd\xi, \tag{15c}$$

$$\mathbf{k}_s^e = \int_{-1}^{1} \mathbf{B}_s^{e^T} GA_s\mathbf{B}_s^e Jd\xi, \tag{15d}$$

where $\mathbf{k}_m^{\mathbf{e}}$ is the $3n \times 3n$ element membrane stiffness matrix, $\mathbf{k}_b^{\mathbf{e}}$ is the $3n \times 3n$ element bending stiffness matrix, and $\mathbf{k}_s^{\mathbf{e}}$ is the $3n \times 3n$ element shearing stiffness matrix. Notation A in Eq. (15a) denotes the assembling algorithm in the framework of the K-FEM, which includes all nodes in the element DOI (not only the element nodes as in the assembly procedure of standard FEM). In Eqs. (15b)–(15d), $\mathbf{B}_m^{\mathbf{e}}$, $\mathbf{B}_b^e$, and $\mathbf{B}_s^e$ are matrices relating the discretized membrane strain, bending strain, and shearing strain, respectively, as defined in Eqs. (1a)–(1c), to the nodal displacement vector defined in Eq. (6), viz.

$$\mathbf{B}_m^{\mathbf{e}} = \begin{bmatrix} \lambda_{1,s} & \dfrac{\lambda_1}{R} & 0 & \lambda_{2,s} & \dfrac{\lambda_2}{R} & 0 & \dots & \lambda_{n,s} & \dfrac{\lambda_n}{R} & 0 \end{bmatrix}, \tag{16a}$$

$$\mathbf{B}_b^e = \begin{bmatrix} 0 & 0 & -\lambda_{1,s} & 0 & 0 & -\lambda_{2,s} & \dots & 0 & 0 & -\lambda_{n,s} \end{bmatrix}, \tag{16b}$$

$$\mathbf{B}_s^e = \begin{bmatrix} -\dfrac{\lambda_1}{R} & \lambda_{1,s} & -\lambda_1 & -\dfrac{\lambda_2}{R} & \lambda_{2,s} & -\lambda_2 & \dots & -\dfrac{\lambda_n}{R} & \lambda_{n,s} & -n \end{bmatrix}. \tag{16c}$$

Symbol J represents the Jacobian of the Kriging-based isoparametric mapping, i.e.,

$$J = s_{,\xi} = \sum_{i=1}^{n} \lambda_{i,\xi} s_i. \tag{17}$$

The global equivalent nodal force vectors $\mathbf{F}_{qs}$, $\mathbf{F}_{qz}$, and $\mathbf{F}_m$ are given as

$$\mathbf{F}_{q_s} = A_{e=1}^{N_e}\mathbf{f}_{q_s}^e, \quad \mathbf{f}_{q_s}^e = \int_{-1}^{1} \mathbf{\Lambda}_u^{\mathrm{T}} q_{\mathrm{s}} Jd\xi, \tag{18a}$$

$$\mathbf{F}_{q_z} = A_{e=1}^{N_e}\mathbf{f}_{q_z}^e, \quad \mathbf{f}_{q_z}^e = \int_{-1}^{1} \mathbf{\Lambda}_w^{\mathrm{T}} q_{\mathrm{z}} Jd\xi, \tag{18b}$$

$$\mathbf{F}_m = A_{e=1}^{N_e}\mathbf{f}_m^e, \quad \mathbf{f}_m^e = \int_{-1}^{1} \mathbf{\Lambda}_\psi^{\mathrm{T}} m Jd\xi. \tag{18c}$$

4. DSG Technique

The Kriging-based curved beam elements with exact integration of all integrals, may exhibit shear locking and membrane locking. In this section, we address the application of the DSG technique [Koschnick *et al.* (2005)] to circumvent the locking phenomena.

4.1. *DSG technique to eliminate shear locking*

The basic idea behind the DSG technique is to modify the expression for the troublesome, constrained displacement-based strain into a strain obtained from the derivatives of a DSG's interpolation [Bischoff *et al.* (2003); Bletzinger *et al.* (2000); Koschnick *et al.* (2005)]. To circumvent shear locking, the first step is to define a shear gap field and the corresponding DSG (in this context, DSG stands for DSG). A 'shear gap' Δw_γ at a point with coordinate $\hat{s}$, is defined as the increment of the radial displacement due to shear deformation at point $\hat{s}$ from a reference point s_0, that is,

$$\Delta w_\gamma(\hat{s}) = \int_{s_0}^{\hat{s}} \gamma_{sz} ds = \int_{s_0}^{\hat{s}} w_{,s}(s) ds - \int_{s_0}^{\hat{s}} \psi(s) ds - \int_{s_0}^{\hat{s}} \frac{u(s)}{R} ds. \tag{19}$$

Furthermore, a DSG is defined as the shear gap at an element *nodal point*, i.e.,

$$\Delta w_{\gamma i} = \Delta w_\gamma(s_i) = w|_{s_0}^{s_i} - \int_{s_0}^{s_i} \psi ds - \int_{s_0}^{s_i} \frac{u}{R} ds, \tag{20}$$

where s_i is the coordinate location of nodal point $i = j, j+1$. Indices j and $j+1$ here represent the element node numbers following the local DOI numbering system, e.g., $j = 2$ and $j + 1 = 3$ for a two-layer DOI (see Figs. 3 and 4). These indices are defined only for element node numbers and are not for any satellite nodes.

The second step is to construct a *substitute* shear gap field for each element by interpolating the DSGs at the element nodal points, i.e.,

$$\Delta \overline{w}_\gamma(\xi) = \sum_{i=j}^{j+1} N_i^e(\xi) \Delta w_{\gamma i}, \tag{21}$$

where $N_i^e(\xi)$, $i = j, j+1$ are shape functions for the substitute shear gap. Following Wong *et al.* [2022], the $N_i^e(\xi)$'s are taken to be the standard linear shape functions,[a] irrespective of the polynomial basis and correlation functions used in the Kriging shape functions. A substitute *shear strain* field is then obtained by differentiating the substitute shear gap field, Eq. (21), with respect to s, viz.

$$\overline{\gamma}(\xi) = \sum_{i=j}^{j+1} N_i^e{}_{,s} \Delta w_{\gamma i} = \bar{\mathbf{B}}_{s1}^{\mathbf{e}} \Delta \mathbf{w}_\gamma^{\mathbf{e}}, \tag{22a}$$

---

[a]We deliberately chose not to use the same Kriging shape functions for interpolating DSGs as those used for interpolating nodal displacements because Wong *et al.* [2018; 2022] showed that the use of Kriging shape functions for interpolating DSGs does not entirely 'unlock' the Kriging-based Timoshenko beam elements.

F. T. Wong & J. Gunawan

$$\bar{\mathbf{B}}_{s1}^{\mathbf{e}} = [N_j^e{}_{,s} \quad N_{j+1,s}^e] = \frac{1}{L^e}[-1 \quad 1], \tag{22b}$$

$$\mathbf{\Delta w}_\gamma^{\mathbf{e}} = [\Delta w_{\gamma j} \quad \Delta w_{\gamma j+1}]^{\mathrm{T}}. \tag{22c}$$

Taking node 1 in the DOI as the reference point and inserting Eqs. (5a)–(5c) into Eq. (20), the DSG values at nodal points $i = j$ and $j + 1$ in the DOI can be expressed as

$$\Delta w_{\gamma i} = (w_i - w_1) - \left(\int_{\xi_1}^{\xi_i} \mathbf{\Lambda}_\psi J d\xi\right) \mathbf{d^e} - \left(\int_{\xi_1}^{\xi_i} \frac{1}{R} \mathbf{\Lambda}_u J d\xi\right) \mathbf{d^e}. \tag{23}$$

Hence, the vector of DSGs, $\mathbf{\Delta w}_\gamma^{\mathbf{e}}$, can be expressed as

$$\Delta \mathbf{w}_\gamma^{\mathbf{e}} = \bar{\mathbf{B}}_{s2}^{\mathbf{e}} \mathbf{d^e}, \tag{24a}$$

where

$$\bar{\mathbf{B}}_{s2}^{\mathbf{e}}$$

$$= \begin{bmatrix} -\int_{\xi_1}^{\xi_j} \frac{1}{R}\lambda_1 J d\xi & -1 -\int_{\xi_1}^{\xi_j} \lambda_1 J d\xi & -\int_{\xi_1}^{\xi_j} \frac{1}{R}\lambda_2 J d\xi & 0 & -\int_{\xi_1}^{\xi_j} \lambda_2 J d\xi & \cdots \\ -\int_{\xi_1}^{\xi_{j+1}} \frac{1}{R}\lambda_1 J d\xi & -1 -\int_{\xi_1}^{\xi_{j+1}} \lambda_1 J d\xi & -\int_{\xi_1}^{\xi_{j+1}} \frac{1}{R}\lambda_2 J d\xi & 0 & -\int_{\xi_1}^{\xi_{j+1}} \lambda_2 J d\xi & \cdots \end{bmatrix}$$

$$\begin{matrix} -\int_{\xi_1}^{\xi_j} \frac{1}{R}\lambda_j J d\xi & 1 -\int_{\xi_1}^{\xi_j} \lambda_j J d\xi & \cdots & -\int_{\xi_1}^{\xi_j} \frac{1}{R}\lambda_n J d\xi & 0 & -\int_{\xi_1}^{\xi_j} \lambda_n J d\xi \\ -\int_{\xi_1}^{\xi_{j+1}} \frac{1}{R}\lambda_j J d\xi & 1 -\int_{\xi_1}^{\xi_{j+1}} \lambda_j J d\xi & \cdots & -\int_{\xi_1}^{\xi_{j+1}} \frac{1}{R}\lambda_n J d\xi & 0 & -\int_{\xi_1}^{\xi_{j+1}} \lambda_n J d\xi \end{matrix} \Bigg].$$

$$\tag{24b}$$

Substituting Eq. (24a) into Eq. (22a) yields

$$\overline{\gamma}(\xi) = \bar{\mathbf{B}}_{s1}^{\mathbf{e}} \bar{\mathbf{B}}_{s2}^{\mathbf{e}} \mathbf{d}^e = \bar{\mathbf{B}}_s^{\mathbf{e}} \mathbf{d}^e. \tag{25}$$

Therefore, to circumvent shear locking, the shear strain-displacement matrix $\mathbf{B}_s^e$ in the shearing stiffness matrix, Eq. (15d), is replaced with $\bar{\mathbf{B}}_s^{\mathbf{e}}$ defined in Eq. (25).

4.2. *DSG technique to eliminate membrane locking*

Applying the same concept to the membrane strain, Eq. (1a), 'membrane strain gap' Δu_ε at a point with coordinate $\hat{s}$ is defined as

$$\Delta u_\varepsilon(\hat{s}) = \int_{s_0}^{\hat{s}} \varepsilon_m ds = \int_{s_0}^{\hat{s}} u_{,s}(s) ds + \int_{s_0}^{\hat{s}} \frac{w(s)}{R} ds. \tag{26}$$

A *discrete* membrane strain gap (DSG) is the membrane strain gap at an element nodal point, i.e.,

$$\Delta u_{\varepsilon i} \equiv \Delta u_\varepsilon(s_i) = u(s)|_{s_0}^{s_i} + \int_{s_0}^{s_i} \frac{w(s)}{R} ds, \tag{27}$$

where s_i is the coordinate location of the nodal point number $i = j$, $j + 1$ (following the local DOI numbering system).

A *substitute* membrane strain gap field over an element is obtained by interpolating DSGs at the element nodal points, viz.

$$\Delta \overline{u}_\varepsilon(\xi) = \sum_{i=j}^{j+1} N_i^e(\xi) \Delta u_{\varepsilon i}. \tag{28}$$

Here, $N_i^e(\xi)$, $i = j, j+1$ are shape functions for the substitute membrane strain gap, which are the standard linear shape functions (identical to those for the substitute shear gap interpolation). A substitute membrane strain field is then obtained by differentiating Eq. (28) with respect to s, i.e.,

$$\overline{\varepsilon}(\xi) = \sum_{i=j}^{j+1} N_i^e{,}_s \Delta u_{\varepsilon i} = \bar{\mathbf{B}}_{m1}^{\mathbf{e}} \Delta \mathbf{u}_\varepsilon^{\mathbf{e}}, \tag{29a}$$

$$\bar{\mathbf{B}}_{m1}^{\mathbf{e}} = [N_j^e{,}_s \quad N_{j+1}^e{,}_s] = \frac{1}{L^e}[-1 \quad 1], \tag{29b}$$

$$\Delta \mathbf{u}_\varepsilon^{\mathbf{e}} = [\Delta u_{\varepsilon j} \quad \Delta u_{\varepsilon j+1}]^{\mathrm{T}}. \tag{29c}$$

Taking node 1 in the DOI as the reference point and inserting Eqs. (5a)–(5c) into Eq. (27), the DSG values at nodal points $i = j$, $j + 1$ in the DOI can be expressed as

$$\Delta u_{\varepsilon i} = (u_i - u_1) + \left(\int_{\xi_1}^{\xi_i} \frac{1}{R} \mathbf{\Lambda}_w J \, d\xi \right) \mathbf{d}^{\mathbf{e}}. \tag{30}$$

Hence, the vector of DSGs, $\Delta \mathbf{u}_\varepsilon^{\mathbf{e}}$, can be expressed as

$$\Delta \mathbf{u}_\varepsilon^{\mathbf{e}} = \bar{\mathbf{B}}_{m2}^{\mathbf{e}} \mathbf{d}^{\mathbf{e}}, \tag{31a}$$

where

$$\bar{\mathbf{B}}_{m2}^{\mathbf{e}} = \begin{bmatrix} -1 & \int_{\xi_1}^{\xi_j} \frac{1}{R}\lambda_1 J \, d\xi & 0 & 0 & \int_{\xi_1}^{\xi_j} \frac{1}{R}\lambda_2 J \, d\xi & 0 & \cdots \\ -1 & \int_{\xi_1}^{\xi_{j+1}} \frac{1}{R}\lambda_1 J \, d\xi & 0 & 0 & \int_{\xi_1}^{\xi_{j+1}} \frac{1}{R}\lambda_2 J d\xi & 0 & \cdots \end{bmatrix}$$

$$\left. \begin{matrix} 1 & \int_{\xi_1}^{\xi_j} \frac{1}{R}\lambda_j J \, d\xi & 0 & \cdots & 0 & \int_{\xi_1}^{\xi_j} \frac{1}{R}\lambda_n J \, d\xi & 0 \\ 1 & \int_{\xi_1}^{\xi_{j+1}} \frac{1}{R}\lambda_j J \, d\xi & 0 & \cdots & 0 & \int_{\xi_1}^{\xi_{j+1}} \frac{1}{R}\lambda_n J \, d\xi & 0 \end{matrix} \right]. \tag{31b}$$

Substituting Eq. (31a) into Eq. (29a) yields

$$\overline{\varepsilon}(\xi) = \bar{\mathbf{B}}_{m1}^{\mathbf{e}} \bar{\mathbf{B}}_{m2}^{\mathbf{e}} \mathbf{d}^e = \bar{\mathbf{B}}_m^{\mathbf{e}} \mathbf{d}^e. \tag{32}$$

Therefore, to avoid membrane locking with the DSG concept, the membrane strain–displacement matrix $\mathbf{B}_m$ in the membrane stiffness matrix, Eq. (15b), is replaced with the substitute membrane strain–displacement matrix $\bar{\mathbf{B}}_m^{\mathbf{e}}$ given in Eq. (32).

F. T. Wong & J. Gunawan

5. Numerical Tests

The Kriging-based curved beam elements with the DSG techniques (referred to as K-Cbeam-DSG elements) addressed in the previous sections have been coded using MATLAB software. In this section, we present a series of numerical tests to evaluate the element performance[b], in terms of locking-free characteristics, accuracy, and convergence. Five problems of curved beam structures were selected to test the curved beam elements, namely: (1) a quarter circular cantilever arch with various thicknesses, (2) a pinched ring, (3) a ring under uniform internal pressure, (4) a quarter circular simply supported arch under a central moment load, and (5) a cantilever beam with spiral geometry. The shapes of the beam cross-section are rectangular. Accordingly, the shear correction factor is taken to be 5/6.

In these numerical tests, the integrals in the element stiffness matrices, Eqs. (15b)–(15d), in the element equivalent nodal force vectors, Eqs. (18a)–(18c), and in the DSG-displacement matrices, Eqs. (24b) and (31b), were all numerically evaluated using the Gauss–Legendre quadrature rule. The number of quadrature sampling points was taken to be three for all integral expressions. This number of sampling points was chosen after several trials, to find the lowest but reasonably accurate number of sampling points.

Different types of the K-Cbeam-DSG elements considered in this study are those using a linear to cubic basis function with the number of element layers ranging from one to three, and using the gaussian (G), Eq. (11a), and QS, Eq. (11b), correlation functions. The correlation parameters, θ_r, were taken to be the mid-value between the lower and upper bounds given in Wong *et al.* [2018], Wong and Syamsoeyadi [2011]. However, only the results obtained using the K-Cbeam-DSG with the G correlation function were reported here, for the sake of brevity, because the results using the QS correlation function were found to be very similar to those using the G correlation function (that is, have the same locking-free and convergence characteristics). The notation used to denote different types of the K-Cbeam-DSG elements is of the form P(a)-(b)-(c), where:

‘(a)’ denotes the polynomial basis—1: linear, 2: quadratic, 3: cubic,
‘(b)’ denotes the number of element layers in the DOI,
‘(c)’ denotes the type of correlation function—G: gaussian, QS.

For example, P2-2-G means that it is the K-Cbeam-DSG element with a quadratic basis function, two element layers of the DOI (see Fig. 4), and the G correlation function.

---

[b]The performance of Kriging-based beam elements without the DSG technique is not considered in this study since it has been previously examined in Wong *et al.* (2018), Wong and Syamsoeyadi (2011), in the framework of the straight Timoshenko beam model. The Kriging-based beam elements without any locking treatment perform poorly due to the locking phenomenon, in particular when they are applied to thin beams.

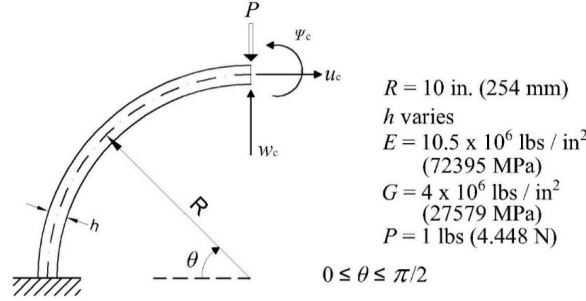*Locking-Free Kriging-Based Curved Beam Elements*

Fig. 5. A quarter circular cantilever arch.

5.1. *A quarter circular cantilever arch with various thicknesses*

To examine whether the DSG techniques in the proposed elements are effective in eliminating the shear locking and membrane locking phenomena, we used the quarter circular cantilever arch shown in Fig. 5 as a test problem. The radius-to-thickness ratio of this arch varies from $R/h = 4$ (a thick arc) to $R/h = 10,000$ (an extremely thin arch). The cross-section of the arch is rectangular with a unit width. The cantilever arc problem has been employed by many researchers to study locking effects [Kim and Kim (1998); Kim and Park (2006); Lee and Sin (1994); Nascimbene (2013); Raveendranath *et al.* (1999, 2001) ; Saleeb and Chang (1987); Yang *et al.* (2014)]. The exact tip displacement components derived using the Castigliano or unit load theorem are given as

$$w_{\rm c} = -\left(\frac{\pi PR^3}{4EI} + \frac{\pi PR}{4GA_{\rm s}} + \frac{\pi PR}{4EA}\right), \tag{33a}$$

$$u_{\rm c} = \frac{PR^3}{2EI} + \frac{PR}{2GA_{\rm s}} - \frac{PR}{2EA}, \tag{33b}$$

$$\psi_{\rm c} = -\frac{PR^2}{EI}. \tag{33c}$$

It is noteworthy that the second term of u_c, Eq. (33b), was mistakenly written as a term with a negative sign in Lee and Sin [1994], Nascimbene [2013], Raveendranath *et al.* [1999], Yang *et al.* [2014].

The cantilever arch was modeled using four identical K-Cbeam-DSG elements of the P1-2-G, P1-3-G, P2-2-G, and P3-3-G types. The results of the tangential displacement, radial displacement, and cross-section rotation at the free end (normalized to the corresponding exact solutions) are presented in Tables 2 and 3. The tables show that the results are stable over the entire range of the radius-to-thickness ratios, without exhibiting any deterioration in the thin regime. Therefore, the K-Cbeam-DSG elements of all types are, indeed, free from any locking. Moreover, they yield remarkably accurate results for the entire range of beam thickness.

Table 2. Normalized tip displacements of the quarter circular cantilever arch for different radius-to-thickness ratios, obtained using four K-Cbeam-DSG elements with a linear basis function.

	P1-2-G			P1-3-G		
R/h	u/u_c	w/w_c	ψ/ψ_c	u/u_c	w/w_c	ψ/ψ_c
4	0.99742	0.99882	0.99945	0.99644	0.99660	0.99772
10	0.99754	0.99857	0.99945	0.99652	0.99635	0.99772
20	0.99755	0.99853	0.99945	0.99653	0.99632	0.99772
50	0.99756	0.99852	0.99945	0.99653	0.99631	0.99772
100	0.99756	0.99852	0.99945	0.99653	0.99631	0.99772
1000	0.99756	0.99852	0.99945	0.99653	0.99631	0.99772
10000	0.99756	0.99852	0.99945	0.99653	0.99631	0.99772

Table 3. Normalized tip displacements of the quarter circular cantilever arch for different radius-to-thickness ratios, obtained using four K-Cbeam-DSG elements with quadratic and cubic basis functions.

	P2-2-G			P3-3-G		
R/h	u/u_c	w/w_c	ψ/ψ_c	u/u_c	w/w_c	ψ/ψ_c
4	0.99733	0.99869	0.99934	1.00042	1.00229	1.00043
10	0.99745	0.99844	0.99934	1.00055	1.00202	1.00043
20	0.99746	0.99840	0.99934	1.00057	1.00198	1.00043
50	0.99747	0.99839	0.99934	1.00057	1.00197	1.00043
100	0.99747	0.99839	0.99934	1.00057	1.00197	1.00043
1000	0.99747	0.99839	0.99934	1.00057	1.00197	1.00043
10000	0.99747	0.99839	0.99934	1.00057	1.00197	1.00043

5.1.1. *Distributions of axial force and shear force*

To study whether the K-Cbeam-DSG elements satisfy the consistency paradigm as described in Babu and Prathap [1986], Prathap [1994] , Prathap and Babu [1986], we examined the distributions of the stress resultants associated with the constrained strain fields, i.e., the axial force and shear force distributions. Lack of consistency in the interpolations of the membrane strain field or shear strain field will cause severe spurious oscillations in the axial and shear force fields, particularly for a thin curved beam. The analytical axial force and shear force fields of the quarter circular arch (Fig. 5) are given as

$$N = -P\cos\theta, \quad 0 \le \theta \le \pi/2, \tag{34a}$$

$$V = -P\sin\theta, \quad 0 \le \theta \le \pi/2. \tag{34b}$$

The axial force and shear force distributions for the case of the extremely thin cantilever arch ($R/h = 10,000$), obtained using the model of four K-Cbeam-DSG elements of different types, are shown in Figs. 6(a) and 6(b), respectively, alongside their corresponding exact distributions. The graphs of the finite element results

Table 4. Axial force values (normalized to P) over K-Cbeam-DSG elements of different types in the Kriging-based finite element model of the cantilever arch of $R/h = 10,000$.

Element	P1-2-G	P1-3-G	P2-2-G	P3-3-G
1	−0.9853	−0.9783	−0.9852	−0.9810
2	−0.8388	−0.8394	−0.8378	−0.8444
3	−0.5728	−0.5773	−0.5743	−0.5833
4	−0.1481	−0.1457	−0.1475	−0.1388

Table 5. Shear force values (normalized to P) over K-Cbeam-DSG elements of different types in the Kriging-based finite element model of the cantilever arch of $R/h = 10,000$.

Element	P1-2-G	P1-3-G	P2-2-G	P3-3-G
1	−0.1487	−0.1479	−0.1481	−0.1384
2	−0.5733	−0.5792	−0.5749	−0.5830
3	−0.8391	−0.8407	−0.8382	−0.8442
4	−0.9854	−0.9786	−0.9853	−0.9809

were made by taking 11 sampling points over each element. It is seen that the stress resultant distributions from different types of the K-Cbeam-DSG elements are nearly identical, appearing as piecewise constants. Additionally, the constant values of the axial force and shear force for each element are listed in Tables 4 and 5 to distinguish the differences in the results obtained using different K-Cbeam-DSG element types. The results demonstrate that even though the cantilever arc beam under consideration is extremely thin, there is no spurious oscillation in the axial and shear force distributions. Thus, it is evident that the Kriging-based curved beam formulation is consistent with the physical inextensional bending constraint and the Kirchhoff constraint. In other words, the K-Cbeam-DSG elements satisfy Prathap's consistency criterion [Prathap (1994)].

5.1.2. *Convergence test*

To examine the convergence of the K-Cbeam-DSG element results, we reanalyzed the thick arch ($R/h = 4$) and the extremely thin arch ($R/h = 10,000$) using 8 and 16 equal-length elements. The results are presented in Tables 6 and 7, together with those previously obtained using four elements. Overall, the results for both arc thicknesses converge to the analytical values. The results obtained using the P1-3-G and P2-2-G converge monotonically from higher values to lower values, while those obtained using the P3-3-G converge monotonically from higher values

F. T. Wong & J. Gunawan
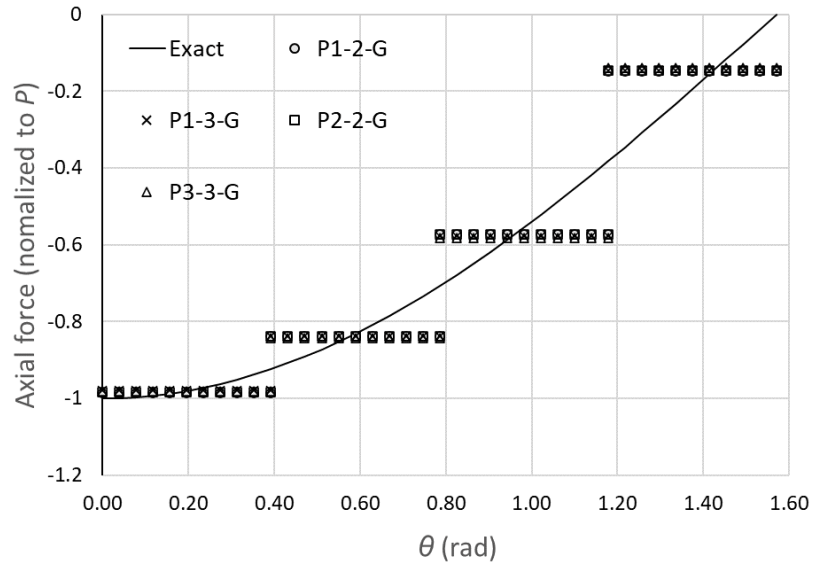
(a)
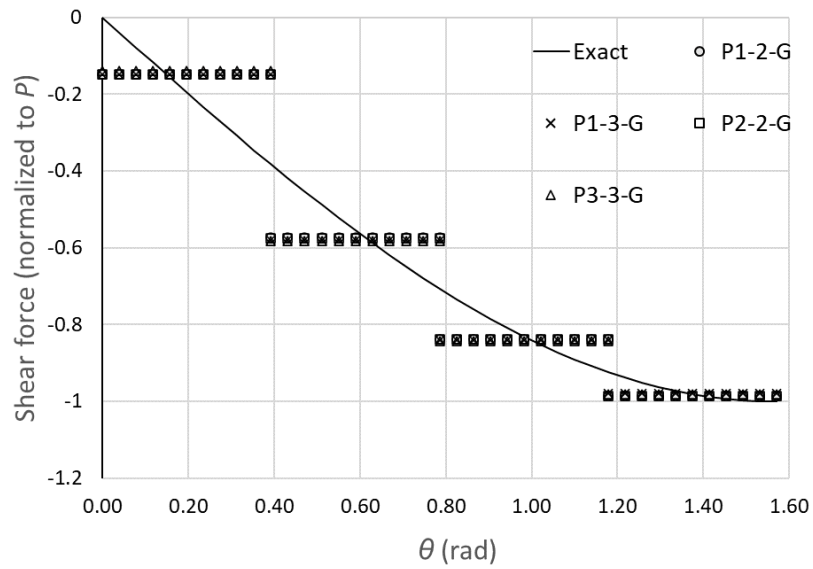
(b)

Fig. 6. (a) Distribution of axial force along the cantilever arch ($R/h = 10,000$) obtained using different types of four K-Cbeam-DSG elements and (b) Distribution of shear force along the cantilever arch ($R/h = 10,000$) obtained using different types of four K-Cbeam-DSG elements.

Table 6. Normalized tip displacements of the quarter circular cantilever arch for the radius-to-thickness ratios 4 and 10,000, obtained using different number of K-Cbeam-DSG elements with a linear basis function.

Number of elements	P1-2-G			P1-3-G		
	u/uc	w/wc	$\psi/\psi c$	u/uc	w/wc	$\psi/\psi c$
$R/h = 4$						
4	0.99742	0.99882	0.99945	0.99644	0.99660	0.99772
8	0.99994	1.00026	1.00010	0.99934	0.99932	0.99963
16	1.00004	1.00011	1.00005	0.99990	0.99991	0.99995
$R/h = 10,000$						
4	0.99756	0.99852	0.99945	0.99653	0.99631	0.99772
8	0.99998	1.00019	1.00010	0.99936	0.99925	0.99963
16	1.00005	1.00009	1.00005	0.99990	0.99989	0.99995

Table 7. Normalized tip displacements of the quarter circular cantilever arch for the radius-to-thickness ratios 4 and 10,000, obtained using different number of K-Cbeam-DSG elements with a quadratic basis and a cubic basis.

Number of elements	P2-2-G			P3-3-G		
	u/uc	w/wc	$\psi/\psi c$	u/uc	w/wc	$\psi/\psi c$
$R/h = 4$						
4	0.99733	0.99869	0.99934	1.00042	1.00229	1.00043
8	0.99979	1.00000	0.99996	0.99999	1.00015	1.00002
16	0.99998	1.00001	1.00000	0.99999	1.00002	1.00000
$R/h = 10,000$						
4	0.99747	0.99839	0.99934	1.00057	1.00197	1.00043
8	0.99983	0.99993	0.99996	1.00003	1.00008	1.00002
16	0.99999	1.00000	1.00000	1.00000	1.00000	1.00000

to lower values. It is seen that the results obtained using the P1-2-G converge nonmonotonically.

5.2. *A pinched ring*

A thin ring subjected to an equal radial load at the top and bottom of the ring (as shown in Fig. 7(a)) has become a *de facto* benchmark problem, to test the performance of curved beam elements in a deep arch configuration. After the problem was first introduced and used by Babu and Prathap [1986] to test their elements, the pinched ring has been employed by many researchers to test various curved beam elements [Choi and Lim (1995); Kim and Kim (1998); Kim and Park (2006, 2008); Koziey and Mirza (1994); Lee and Sin (1994); Nascimbene (2013); Prathap and Babu (1986); Raveendranath *et al.* (1999, 2001); Ryu and Sin (1996); Yang *et al.* (2014)]. Due to symmetry, the ring can be modeled using a quarter of the ring with appropriate boundary conditions, as shown in Fig. 7(b).

F. T. Wong & J. Gunawan
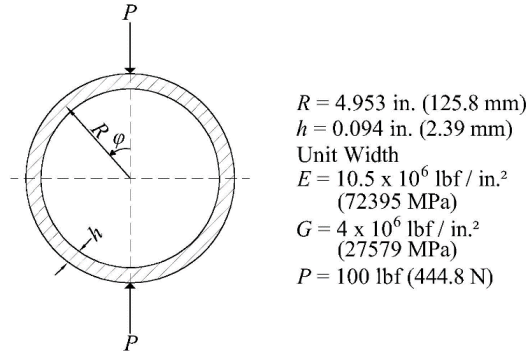
(a)
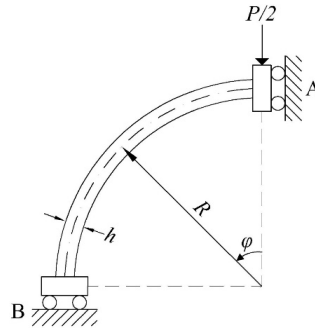
(b)

Fig. 7. (a) A ring subjected to a pair of pinching loads P. (b) A quarter model of the pinched ring (Fig. 7(a)).

Using Castigliano's theorem, the radial displacement (deflection) under a point load at A can be obtained as Lee and Sin [1994], Nascimbene [2013]:

$$w_A = -\left(\frac{(\pi^2-8)PR^3}{8\pi EI} + \frac{\pi PR}{8GA_s} + \frac{\pi PR}{8EA}\right). \tag{35}$$

The analytical bending moment, axial force, and shear force distributions are given as (Nascimbene, 2013; Prathap and Babu, 1986):

$$M = \frac{RP}{2}\left(\sin\varphi - \frac{2}{\pi}\right), \quad 0 \le \varphi \le \pi/2, \tag{36a}$$

$$N = -\frac{P}{2}\sin\varphi, \quad 0 \le \varphi \le \pi/2, \tag{36b}$$

$$V = -\frac{P}{2}\cos\varphi, \quad 0 \le \varphi \le \pi/2. \tag{36c}$$

2nd Reading

Table 8. Normalized deflections under the point load at A of the pinched ring obtained using different numbers and types of K-Cbeam-DSG elements.

No. of elements	P1-2-G	P1-3-G	P2-2-G	P2-3-G	P3-3-G
4	0.9959	0.9958	0.9959	1.0069	1.0075
8	1.0003	0.9985	0.9999	1.0003	1.0003
16	1.0002	0.9998	1.0000	1.0000	1.0000
32	1.0000	1.0000	1.0000	1.0000	1.0000
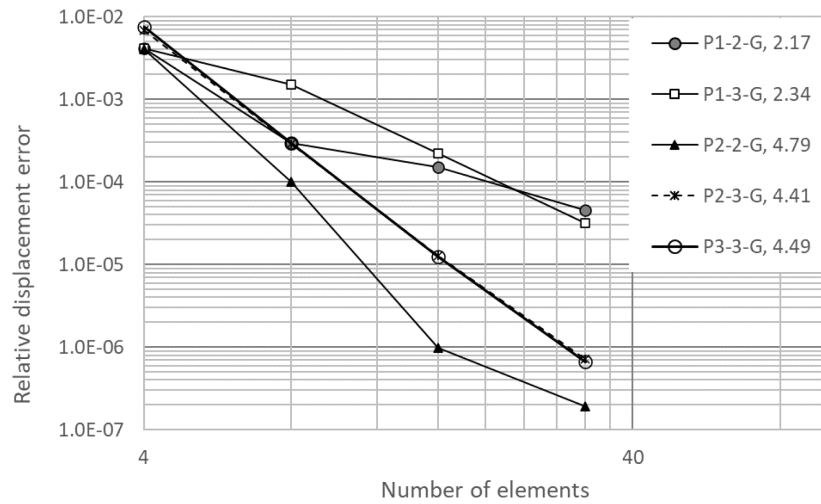
Fig. 8. Relative error displacement versus number of elements for the quadrant of the pinched ring modeled using different types of four identical K-Cbeam-DSG elements. The numbers in the legend indicate the average order of convergence from the model with $N_e = 4$ to $N_e = 32$.

The deflections of the point under the load obtained using different numbers and types of the K-Cbeam-DSG elements, normalized to the exact solution, are listed in Table 8. In addition, the relative errors of the deflection are plotted against the number of elements in Fig. 8. The table and figure demonstrate that all types of the K-Cbeam-DGS elements have excellent accuracy and convergence behavior. Using the model of four curved beam elements, all K-Cbeam-DSG elements produced less than 1% error in deflection. The best accuracy and convergence rate were found in the P2-2-G type, with an average order of convergence of 4.79.

It is worth mentioning that, for K-FEM, similar to the case of 2D problems [Wong and Kanok-Nukulchai (2009a)], increasing the number of the DOI's element layers or increasing the degree of the polynomial basis from a quadratic basis to a cubic or higher basis may not yield better results. In particular, Fig. 8 shows that the results of the P2-3-G and P3-3-G K-Cbeam-DSG elements are less accurate and have a slightly slower convergence rate than those of the P2-2-G element.

Table 9. Normalized deflections under the point load of the pinched ring obtained using a regular mesh and two irregular meshes of four K-Cbeam-DSG elements of different types.

Mesh	P1-2-G	P1-3-G	P2-2-G	P2-3-G	P3-3-G
Regular	0.9959	0.9958	0.9959	1.0069	1.0075
Irregular 1	0.9391	0.9449	0.9393	0.9526	0.9566
Irregular 2	0.8597	0.8735	0.8615	0.8821	0.8874

To assess the accuracy of the stress resultant predictions, the bending moment, axial force, and shear force distributions in the quadrant of the pinched ring, modeled using four K-Cbeam elements of the P1-2-G, P2-2-G, and P3-3G types, were plotted in Figs. 9(a)–9(c). These stress resultants were plotted at 11 points along each element without any smoothing technique. It is seen that the bending moment results of the P1-2-G type are slightly less accurate than those of the P2-2-G and P3-3-G types. In particular, the error of the bending moment at the point under the load obtained using the P1-2-G type is 12%, while those obtained using P2-2-G and P3-3-G types are 1.7% and 1.3%, respectively. The axial force and shear force distributions from the K-Cbeam-DSG element model are piecewise constant, as expected, and have nearly the same accuracy for all types of the K-Cbeam-DSG element.

### 5.2.1. *Sensitivity to mesh distortion*

In the previous analysis, we used regular meshes of K-Cbeam-DSG elements. To investigate the effect of mesh distortion, the pinched ring was reanalyzed using two irregular meshes of four elements as shown in Fig. 10. The normalized deflections of the point under the load are documented in Table 9. Notably, the accuracy of the results decreases as the mesh irregularity increases. Thus, the K-Cbeam-DSG elements' performance is rather sensitive to mesh distortion.

### 5.3. *A ring under uniform internal pressure*

The same symmetric-quarter model ring employed in the previous problem (Fig. 7(b)), was subjected to a uniform internally distributed load of unit magnitude [Raveendranath *et al.* (2001)], i.e., $q_z = 1$ lbf/in (0.1751 N/mm). This test aims to evaluate the performance of the beam elements in a purely extensional problem of curved beams. The analytical solutions for the uniform radial displacement and axial force over the ring are, respectively:

$$w = \frac{q_z R^2}{EA} = 2.48553 \text{ in } (63.1325 \text{ mm}), \tag{37a}$$

$$N = q_z R = 4.953 \text{ lbf } (22.03 \text{ N}). \tag{37b}$$

*Locking-Free Kriging-Based Curved Beam Elements*
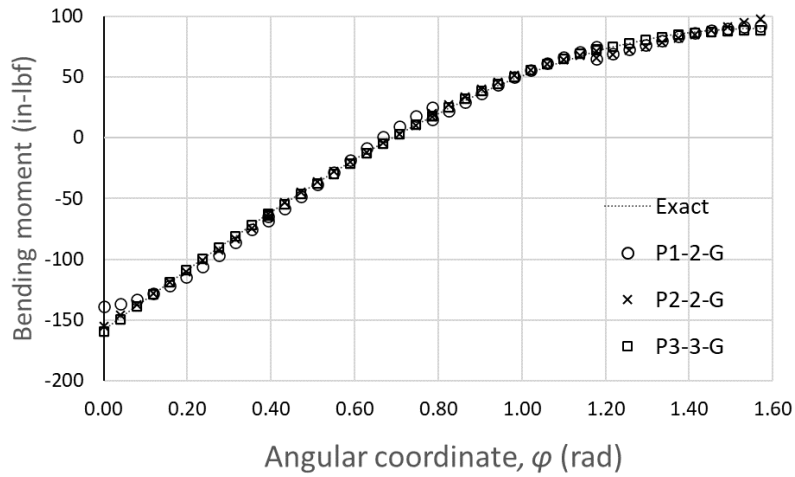
(a)
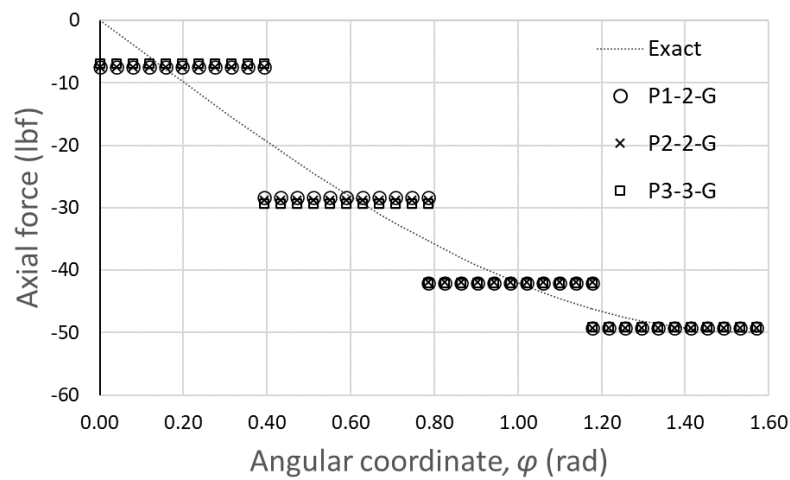
(b)

Fig. 9. (a) Bending moment distributions in a quadrant of the pinched ring obtained using models of four K-Cbeam-DSG elements of P1-2-G, P2-2-G, and P3-3-G. (b) Axial force distributions in a quadrant of the pinched ring obtained using models of four K-Cbeam-DSG elements of P1-2-G, P2-2-G, and P3-3-G. (c) Shear force distributions in a quadrant of the pinched ring obtained using models of four K-Cbeam-DSG elements of P1-2-G, P2-2-G, and P3-3-G.

The analysis using four-element model of the K-Cbeam-DSG elements of types P1-2-G, P1-3G, P2-2-G, P2-3G, and P3-3-G reproduces the exact solutions (Eqs. (37a) and (37b)). These super-accurate results are not surprising because the exact displacement fields in this problem are constant, which can be exactly reproduced.

(c)

Fig. 9. *(Continued)*.
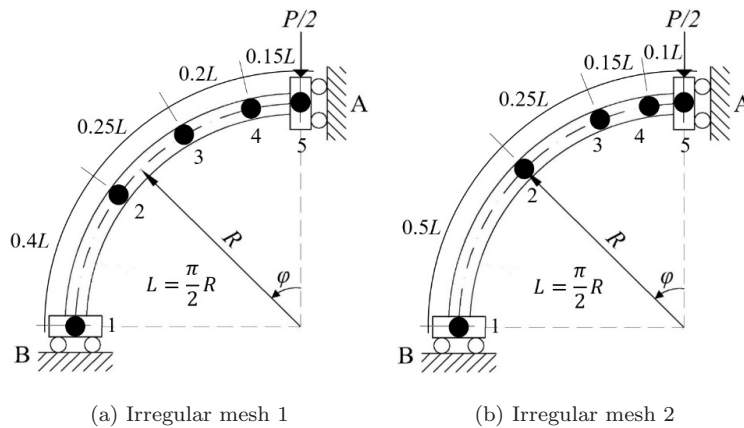

(a) Irregular mesh 1   (b) Irregular mesh 2
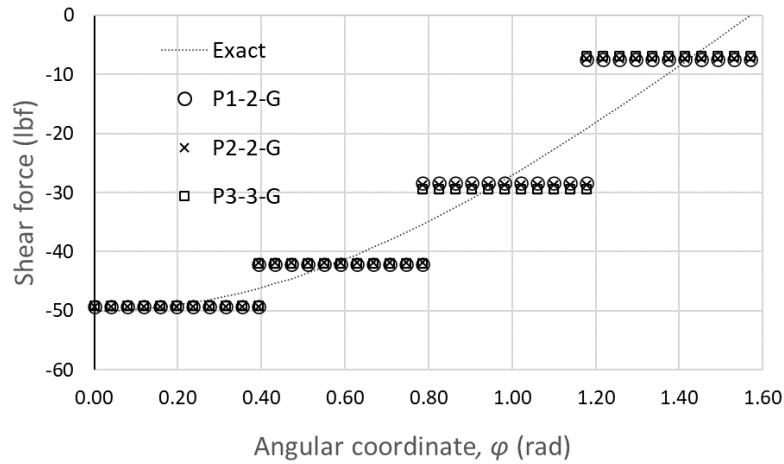
Fig. 10. Two irregular four-element meshes of a quarter of the pinched ring (Fig. 7(b)).

Remark 1

In addition to the pure extensional problem, we tested the K-Cbeam-DSG elements to a problem of pure bending problem, that is, a cantilever curved beam under a tip moment load. For the sake of brevity, the details are not reported here (see a similar pure bending test for a straight Timoshenko beam in Wong *et al.* [2022]. In this pure bending test, the exact solutions can also be reproduced using a minimum number of the K-Cbeam-DSG elements. The pure extensional test and pure bending test can be regarded as patch tests for curved beam elements. Therefore, the K-Cbeam-DSG elements pass the patch test.
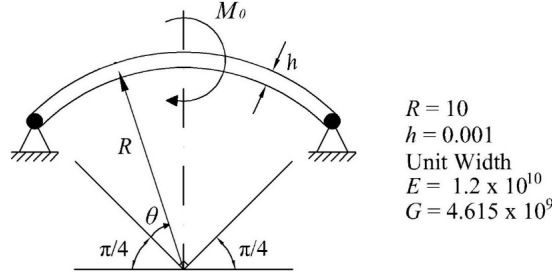
Fig. 11. A quarter circular arch with hinged supports under a concentrated moment load M_o in the middle of the span.

5.4. *A quarter circular simply supported arch under a central moment load*

Figure 11 shows a quarter circular arch with hinged support, subjected to a concentrated moment load M_o in the middle of the span. This problem is intended to test the K-Cbeam-DSG elements in representing a discontinuous bending moment distribution. The analytical solution for the central displacement components, based on the Euler-Bernoulli thin beam theory, is as follows [Lee and Sin (1994); Raveendranath *et al.* (1999)]:

$$u_{EB} = -0.0100489 \frac{M_o R^2}{EI} = -1.00489, \tag{38a}$$

$$w_{EB} = 0, \tag{38b}$$

$$\psi_{EB} = -0.1211846 \frac{M_o R}{EI} = -1.21185. \tag{38c}$$

The analytical solution for the bending moment is given as follows [Kim and Kim (1998); Lee and Sin (1994); Raveendranath *et al.* (1999)]:

$$M = \begin{cases} (1 - \cos\theta + \sin\theta)\dfrac{M_o}{2} & 0 \le \theta < \dfrac{\pi}{4}, \\[3mm] (-1 - \cos\theta + \sin\theta)\dfrac{M_o}{2} & \dfrac{\pi}{4} < \theta \le \dfrac{\pi}{2}. \end{cases} \tag{39}$$

The bending moment is discontinuous at $\theta = \pi/4$.

The simply supported arch (Fig. 11) was analyzed using 4, 8, 16, and 32 K-Cbeam-DSG elements of different types. The resulting tangential displacements and rotations at the middle of the span, normalized to the thin curve beam solutions, are presented in Table 10. The table shows that the axial displacement results are reasonably accurate and converge to the analytical solution. However, the rotation results are not as accurate and exhibit very slow convergence. Even using 32 elements, the results are only about 97% of the analytical solution. The reason for this is that the use of Kriging shape functions with the DOI of two or three layers of elements causes the two elements at the middle of the span, where the concentrated

F. T. Wong & J. Gunawan

Table 10. Normalized tangential displacements, u/u_{EB}, and normalized rotations, ψ/ψ_{EB}, at the middle of the quarter circular simply supported arch subjected to a concentrated moment load, obtained using K-Cbeam-DSG elements (without special treatment for the moment discontinuity problem).

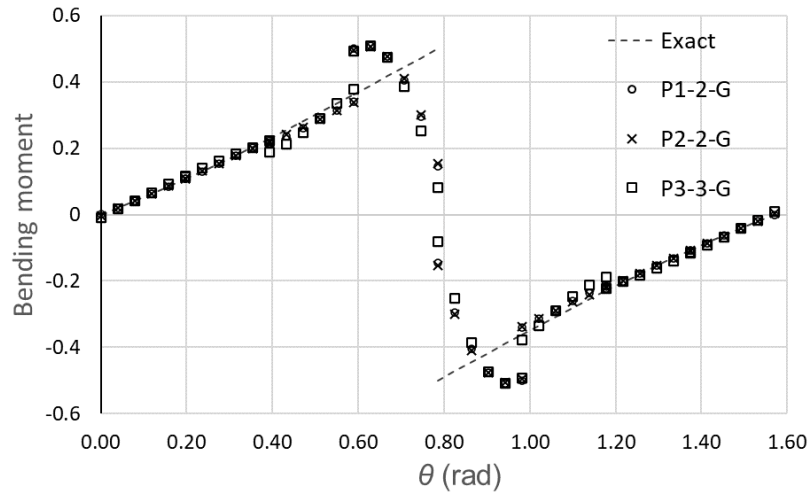| Number of elements	P1-2-G	P1-3-G	P2-2-G	P2-3-G	P3-3-G
(a) u/u_{EB}					
4	0.9953	1.0233	1.0024	1.0425	1.0411
8	0.9948	0.9913	0.9950	0.9943	0.9943
16	0.9992	0.9990	0.9992	0.9993	0.9993
32	0.9999	0.9999	0.9999	0.9999	0.9999
(b) ψ/ψ_{EB}					
4	0.8437	0.6297	0.8490	0.6341	0.6216
8	0.9253	0.8982	0.9300	0.8992	0.8994
16	0.9625	0.9490	0.9653	0.9497	0.9498
32	0.9812	0.9745	0.9827	0.9748	0.9749

Fig. 12. Bending moment distributions in the simply-supported arc subjected to a central moment, obtained using models of eight K-Cbeam-DSG elements (without special treatment for the moment discontinuity problem).

moment is applied at one of their end nodes, to be unable to represent the bending moment discontinuity (see Fig. 12).

To deal with this discontinuity problem properly, the arch structure was re-analyzed by treating the two middle elements as if they were elements at the end, as illustrated in Fig. 13. Therefore, the DOIs of the elements in the left portion and those of the elements in the right portion are separated from each other. The normalized results are shown in Table 11. For the model with four elements,
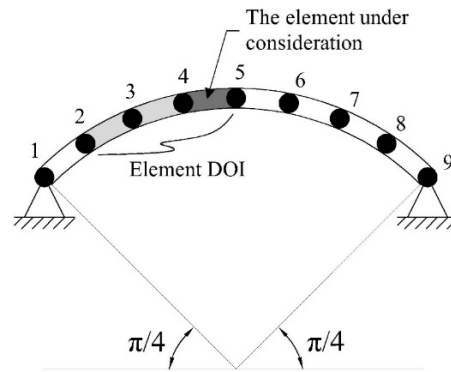
Fig. 13. Illustration of the three-layer DOI for the element at the middle of the span to deal with the moment discontinuity problem. The arch in Fig. 11 was discretized using eight K-Cbeam-DSG elements.
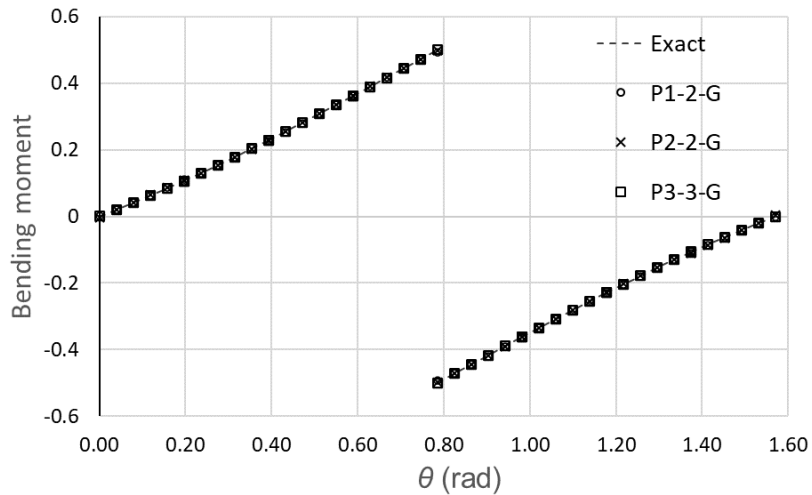

Fig. 14. Bending moment distributions in the simply-supported arc subjected to a central moment, obtained using models of eight Kriging-based curved beam elements with special treatment for the moment discontinuity problem.

the K-Cbeam-DSG element types P1-3-G, P2-3-G, and P3-3-G are not applicable because the minimum number of elements for using these three-layer DOI types is six. Therefore, if the middle elements are treated separately, each portion needs at least three elements. The table shows that the results are now very accurate and converge well toward the analytical solutions. Moreover, the K-Cbeam-DSG elements are able to predict the bending moment distribution accurately, as shown in Fig. 14.

Table 11. Normalized tangential displacements, u/u_{EB}, and normalized rotations, ψ/ψ_{EB}, at the middle of the quarter circular simply-supported arch subjected to a concentrated moment load, obtained using K-Cbeam-DSG elements with special treatment for the moment discontinuity problem.

Number of elements	P1-2-G	P1-3-G	P2-2-G	P2-3-G	P3-3-G
(a) u/u_{EB}					
4	0.9912	N. A.	1.0015	N. A.	N. A.
8	0.9992	0.9903	0.9988	0.9993	0.9995
16	1.0003	0.9987	0.9999	1.0000	1.0000
32	1.0002	0.9998	1.0000	1.0000	1.0000
(b) ψ/ψ_{EB}					
4	0.9955	N. A.	0.9947	N. A.	N. A.
8	0.9997	1.0002	0.9998	1.0002	1.0002
16	0.9999	1.0000	1.0000	1.0000	1.0000
32	1.0000	1.0000	1.0000	1.0000	1.0000

Remark 2

This test problem illustrates that while the K-FEM works well in model problems with smooth solutions, it has difficulty in application to problems that have discontinuous gradients. Therefore, we may expect the K-FEM to perform poorly in problems with discontinuous gradients, such as beams with one or more concentrated loads at the interior points (like in this example) or solid bodies with abrupt changes in the material or geometrical properties. To tackle these problems, the elements and their corresponding DOIs over the discontinuity locations should be cut off, as shown this example. This method of DOI separation has been successfully applied by Sommanawat [2010] to problems of one-and two-dimensional solid bodies with material discontinuities.

The K-FEM can work without any treatment for problems with strong gradients or even infinite gradients (singularity). However, the convergence rate will be slower. For an example of a strong gradient problem solved using the K-FEM, readers can refer to the analysis of an infinite plane-stress plate with a hole presented in Wong and Kanok-Nukulchai [2009a] . Another example of a problem that includes a gradient singularity can be found in the surface fitting analysis of a semi-spherical shell presented in Wong and Kanok-Nukulchai [2009b].

Moreover, the K-FEM can be used to solve problems with strong discontinuities, such as cracks, in a similar way to traditional FEM, for example, using an interelement crack method [Song *et al.* (2008)]. This approach, however, requires a dense distribution of nodes adjacent to the crack tips to capture the stress singularity. An adaptive mesh refinement scheme such as that presented by Handoko and Wong [2023] can be used to obtain an effective mesh. It is also possible to use the K-FEM to discretize the course-scale (continuum) model in the framework of the multiscale
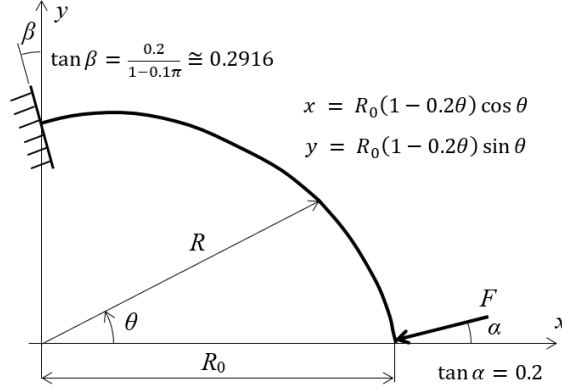
Fig. 15. A cantilever beam with spiral geometry (adopted from Tufekci *et al.*[2017]). The directions of force F and the clamped boundary are perpendicular to the curved beam.

model of material failure [Budarapu *et al.* (2019); Yang *et al.* (2015)]. However, further research is needed in this area.

5.5. *A cantilever beam with spiral geometry*

To test the convergence behavior of the K-Cbeam-DSG elements in a noncircular (nonconstant curvature) case, we take an example of a cantilever beam with spiral geometry presented in Tufekci *et al.* (2017), as shown in Fig. 15. The radius of curvature is defined as

$$R = R_0(1 - \mu\theta), \tag{40}$$

where μ is the shape parameter, θ is the angular coordinate, $0 \leq \theta \leq \pi/2$, and R_0 is the radius of curvature at $\theta = 0$. Numerical data are taken as follows: $\mu = 0.2$, $R_0 = 1\,\mathrm{m}$, $A = 0.01\,\mathrm{m}^2$, $I = 8.333 \times 10^{-6}\,\mathrm{m}^4$, $E = 2 \times 10^{10}\,\mathrm{N/m}^2$, $v = 0.15$, $k = 5/6$ and $F = 1,000N$. The beam is modeled using the K-Cbeam-DSG elements with a constant radius of curvature for each element taken at the element's middle point.

The displacement results at the right endpoint ($R = 1, \theta = 0$) obtained using different numbers and types of the K-Cbeam-DSG elements are presented in Table 12. For comparison, the results obtained using the 'exact' two-node cubic straight beam element (cubic interpolation for w, quadratic for ψ, and linear in u), abbreviated as 2CSB element, are also presented. This 2CSB element is widely used in structural engineering practice and is available in many commercial finite element programs. The results of the model using 32 elements of the four-node cubic curved beam element (consisting of 99 nodal points) with the DSG technique were taken as the reference solutions (since no exact solution is available for this spiral beam). It can be seen that all the K-Cbeam-DSG elements converge well to the corresponding

F. T. Wong & J. Gunawan

Table 12. (a) Tangential displacements (u), (b) radial displacements (w), dan (c) rotation of cross section (ψ) under the point load of the spiral beam obtained using different numbers and types of Kriging-based curved beam elements.

| No. of elements	P1-2-G	P1-3-G	P2-2-G	P2-3-G	P3-3-G	2CSB
(a) Tangential displacement (cm)						
4	0.1891	0.1888	0.1891	0.1894	0.1895	0.1398
8	0.1896	0.1895	0.1896	0.1896	0.1896	0.1677
16	0.1896	0.1896	0.1896	0.1896	0.1896	0.1798
32	0.1896	0.1896	0.1896	0.1896	0.1896	0.1853
32 cubic element	0.1896					
(b) Radial displacement (cm)						
4	−0.3204	−0.3197	−0.3204	−0.3214	−0.3214	−0.3737
8	−0.3223	−0.3220	−0.3222	−0.3222	−0.3222	−0.3502
16	−0.3226	−0.3225	−0.3226	−0.3226	−0.3226	−0.3346
32	−0.3227	−0.3227	−0.3227	−0.3227	−0.3227	−0.3258
32 cubic element	−0.3227					
(c) Rotation (10^{-3} rad)						
4	−4.5874	−4.5786	−4.5868	−4.5899	−4.5902	−4.8840
8	−4.5991	−4.5970	−4.5985	−4.5986	−4.5987	−4.7670
16	−4.6012	−4.6008	−4.6010	−4.6010	−4.6010	−4.6770
32	−4.6016	−4.6015	−4.6016	−4.6016	−4.6016	−4.6230
32 cubic element	−4.6017					

reference solutions. In comparison to the 2CSB element solutions, the K-Cbeam-DSG elements are more accurate in the course mesh and converge faster.

It is worth mentioning here that our reference solutions are a little bit different from those used in Tufekci *et al.* (2017), i.e., $u = 0.1902$ cm, $w = -0.3136$ cm, and $\psi = -4.5606$, which were obtained using the commercial software ABAQUS with 85 B22 beam elements. Compared to these ABAQUS solutions, the converged values of tangential displacement, radial displacement, and rotation at $\theta = 0$ have about -0.31%, 2.89%, and 0.90% differences, respectively.

The averaged nodal bending moments, axial forces, and shear forces along the spiral beam, which were obtained using 18 K-Cbeam-DSG elements of the types P1-2-G, P2-2-G, and P3-3-G, are shown in Figs. 16(a)–16(c). The results are compared to those obtained using 90 2CSB elements in the commercial software SAP2000 and to those obtained using 18 elements of the exact two-node curved beam element as presented in Tufekci *et al.* (2017). It is seen that the internal forces distributions obtained using different types of the K-Cbeam-DSG elements are almost identical and very close to those of the 2CSB elements and Tufekci *et al.* (2017). The exception is at the point $\theta = 0°$ for the axial force and at the point $\theta = 90°$ for the shear force, where at those points, the forces obtained using the K-Cbeam-DSG elements deviate slightly. The reason for this is that at $\theta = 0°$ (or $\theta = 90°$) the nodal axial force (or nodal shear force) is an unaveraged value. It will get better if the mesh is refined.
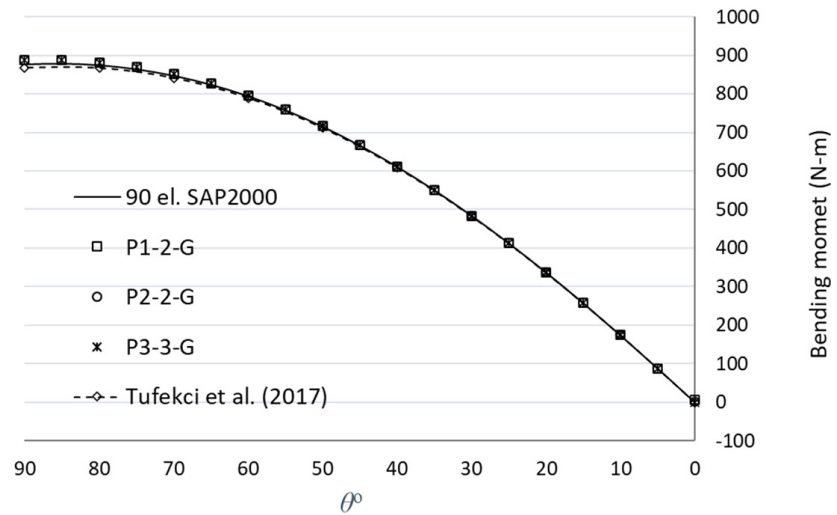
(a)
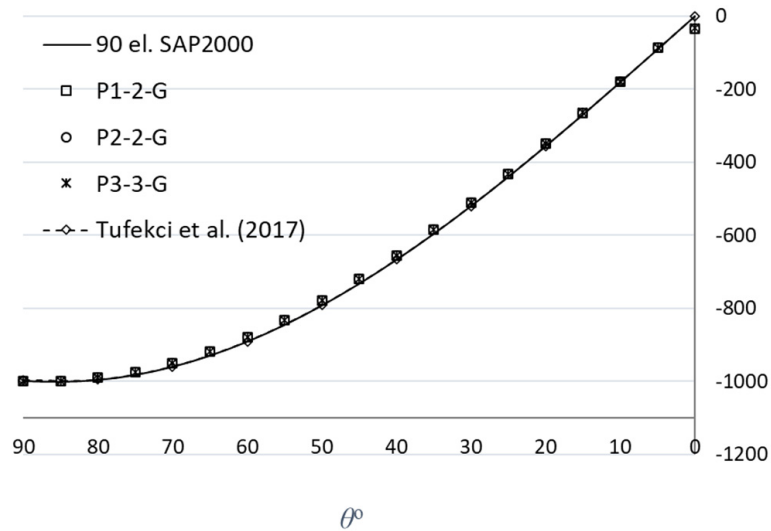
(b)

Fig. 16. (a) Averaged nodal bending moments at the spiral beam obtained using models of 18 K-Cbeam-DSG elements of P1-2-G, P2-2-G, and P3-3-G. (b) Averaged nodal axial forces at the spiral beam obtained using models of 18 K-Cbeam-DSG elements of P1-2-G, P2-2-G, and P3-3-G. (c) Averaged nodal shear forces at the spiral beam obtained using models of 18 K-Cbeam-DSG elements of P1-2-G, P2-2-G, and P3-3-G.

F. T. Wong & J. Gunawan
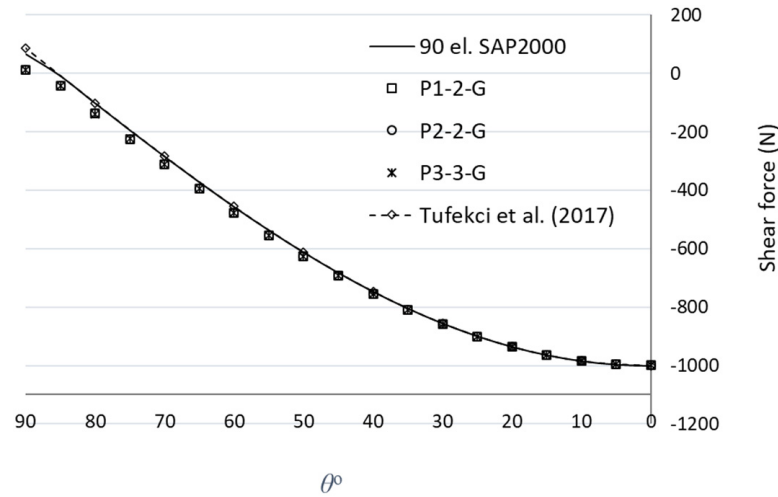
(c)

Fig. 16. (*Continued*)

5.5.1. *Computational efficiency*

To assess the computational efficiency of the K-Cbeam-DSG elements, we conducted computations of the spiral beam using 32 Kriging-based elements of various types and 16 conventional quadratic curved beam elements. We chose this conventional element for a fair comparison because both types of elements have the same degrees of freedom, that is, 96. The computations were carried out on a computer with an Intel Core i7 2.60Ghz processor. The computations were repeated 10 times because we found that the execution time for each computer run varied.

The resulting averaged computational times and a comparison with those of the conventional quadratic element are presented in Table 13. As expected, the K-Cbeam-DSG elements require significantly longer computational time, ranging from tens to hundreds of times longer than the conventional FEM. This is primarily because, as explained in the introductory section, in the K-FEM method, the Kriging shape functions are constructed element by element during the computation. Additionally, the bandwidth of the K-FEM assembled stiffness matrix is larger than that of the conventional FEM because the Kriging shape functions have larger local supports.

Remark 3

Limitations of the geometrical applicability of the present formulation.

The use of curvilinear coordinate, s, in the isoparametric formulation of the K-Cbeam-DSG elements, viz. Eq. (8), and in our MATLAB codes makes the geometry that can be represented by the present formulation limited to curves that have no

Locking-Free Kriging-Based Curved Beam Elements

Table 13. Average running time from 10 times running of the MATLAB codes for the K-Cbeam-DSG element implementation.

	P1-2-G	P1-3-G	P2-2-G	P2-3-G	P3-3-G
Time	0.7969	1.9737	0.8045	2.0468	2.1453
Ratio*	52.3	129.5	52.8	134.2	140.7

*Normalized to running time of spiral beam modeled with 16 quadratic curved beam elements, viz. 0.01525 s.

reversing sign of the curvature. For example, the K-Cbeam-DSG elements cannot solve an S-shaped curved beam, an M-shaped curved beam, or a spring-shaped curved beam as given in Gan [2018]. A straight beam can be handled using a large value of the radius of curvature, R, relative to the beam length. However, the K-Cbeam-DSG elements are not able to handle a skeletal structure composed of several straight beams that make an angle with each other such as the example of a console beam problem presented in Bouclier *et al.* [2012]. The geometrical applicability of the present formulation can be enhanced using global Cartesian coordinates in the isoparametric formulation in place of the curvilinear coordinate (similar to the curved beam formulation in Bouclier *et al.* [2012] in the framework of NURBS-based isogeometric analysis).

6. Conclusion

A family of Kriging-based curved beam elements with the DSG technique (K-Cbeam-DSG elements) have been developed and tested. The test results show that the DSG technique is effective in eliminating both shear locking and membrane locking. Moreover, the K-Cbeam-DSG elements of all types have remarkable accuracy and excellent convergence characteristics over a wide range of thin to thick circular arc beams. The elements, however, are rather sensitive to mesh distortion. In a problem with a bending moment discontinuity, the use of the K-Cbeam-DSG elements needs special treatment. For general noncircular curved beams, the K-Cbeam-DSG elements require a sufficiently fine mesh to achieve high accuracy. The application capability of the presented curved beam elements is limited to curved beams that do not have a reversing curvature.

This study may give insight into developing a locking-free Kriging-based plate and shell elements. Further development of the curved beam elements may be directed toward the improvement of the accuracy for noncircular curved beams, generalization to arbitrary, nonprismatic curved beams, and applications to curved beam dynamic analysis, buckling analysis, and large displacement analysis.

F. T. Wong & J. Gunawan

ORCID

F. T. Wong ⬤ https://orcid.org/0000-0003-3628-8731

Junius Gunawan ⬤ https://orcid.org/0009-0002-2616-6036

References

Babu, C. R. and Prathap, G. [1986] "A linear thick curved beam element," *Int. J. Numer. Methods Eng.* **23**, 1313–1328.

Bischoff, M., Koschnick, F. and Bletzinger, K. [2003] "Stabilized DSG elements–A new paradigm in finite element technology," *Proc. 4th European LS-DYNA Users Conf.*, DYNAmore GmbH, pp. H-I-49–H-I-62.

Bletzinger, K.-U., Bischoff, M. and Ramm, E. [2000] "A unified approach for shear-locking-free triangular and rectangular shell finite elements," *Comput. Struct.* **75**, 321–334.

Bouclier, R., Elguedj, T. and Combescure, A. [2012] "Locking free isogeometric formulations of curved thick beams," *Comput. Methods Appl. Mech. Eng.* **245–246**, 144–162.

Budarapu, P. R., Zhuang, X. Y., Rabczuk, T. and Bordas, S. [2019] "Multiscale modeling of material failure: Theory and computational methods," *Adv. Appl. Mech.* **52**, 1–103.

Choi, J. and Lim, J. [1995] "General curved beam elements based on the assumed strain fields," *Comput. Struct.* **55**, 379–386.

Cook, R. D., Malkus, D. S., Plesha, M. E. and Witt, R. J. [2002] *Concepts and Applications of Finite Element Analysis*, 4th Edition (John Wiley and Sons, Madison).

Cottrell, J. A., Hughes, T. J. R. and Bazilevs, Y. [2009] *Isogeometric Analysis*: *Toward Integration of CAD and FEA* (John Wiley and Sons, Madison).

Cowper, G. R. [1966] "The shear coefficient in Timoshenko's beam theory," *J. Appl. Mech.* **33**, 335–340.

Day, R. A. and Potts, D. M. [1990] "Curved mindlin beam and axi-symmetric shell elements — A new approach," *Int. J. Numer. Methods Eng.* **30**, 1263–1274.

Echter, R. and Bischoff, M. [2010] "Numerical efficiency, locking and unlocking of NURBS finite elements," *Comput. Methods Appl. Mech. Eng.* **199**, 374–382.

Gan, B. S. [2018] *An Isogeometric Approach to Beam Structures* (Springer, Switzerland).

Gu, L. [2003] "Moving kriging interpolation and element-free Galerkin method," *Int. J. Numer. Methods Eng.* **56**, 1–11.

Handoko, J. and Wong, F. T. [2023] "Adaptive mesh refinements for analyses of 2D linear elasticity problems using the Kriging-based finite element method," *E3S Web Conf.* **429**, 05004.

Hughes, T. J. R., Cottrell, J. A. and Bazilevs, Y. [2005] "Isogeometric analysis: CAD, finite elements, NURBS, exact geometry and mesh refinement," *Comput. Methods Appl. Mech. Eng.* **194**, 4135–4195.

Hughes, T. J. R., Taylor, R. L. and Kanok-Nukulchai, W. [1977] "A simple and efficient finite element for plate bending," *Int. J. Numer. Methods Eng.* **11**, 1529–1543.

Kanok-Nukulchai, W., Wong, F. T. and Sommanawat, W. [2015] "Generalization of FEM using node-based shape functions," *Civ. Eng. Dimens.* **17**, 152–157.

Kim, J. G. and Kim, Y. Y. [1998] "A new higher-order hybrid-mixed curved beam element," *Int. J. Numer. Methods Eng.* **43**, 925–940.

Kim, J. G. and Park, Y. K. [2006] "Hybrid-mixed curved beam elements with increased degrees of freedom for static and vibration analyses," *Int. J. Numer. Methods Eng.* **68**, 690–706.

Kim, J. G. and Park, Y. K. [2008] "The effect of additional equilibrium stress functions on the three-node hybrid-mixed curved beam element," *J. Mech. Sci. Technol.* **22**, 2030–2037.

Koschnick, F., Bischoff, M., Camprubí, N. and Bletzinger, K. U. [2005] "The discrete strain gap method and membrane locking," *Comput. Methods Appl. Mech. Eng.* **194**, 2444–2463.

Koziey, B. L. and Mirza, F. A. [1994] "Consistent curved beam element," *Comput. Struct.* **51**, 643–654.

Lee, P. G. and Sin, H. C. [1994] "Locking-free curved beam element based on curvature," *Int. J. Numer. Methods Eng.* **37**, 989–1007.

Liu, G. R. [2016] "An overview on meshfree methods," *Int. J. Comput. Methods* **13**, 1630001-1–1630001-42.

Nascimbene, R. [2013] "An arbitrary cross section, locking free shear-flexible curved beam finite element," *Int. J. Comput. Methods Eng. Sci. Mech.* **14**, 90–103.

Oden, J. T. [1967] *Mechanics of Elastic Structures* (McGraw-Hill, New York).

Olea, R. A. [2018] *A Practical Primer on Geostatistics*, U. S. Geological Survey Open-File Report 2009.

Plengkhom, K. and Kanok-Nukulchai, W. [2005] "An enhancement of finite element method with moving Kriging shape functions," *Int. J. Comput. Methods* **2**, 451–475.

Prathap, G. [1994] "The displacement-type finite element approach—From art to science," *Prog. Aerosp. Sci.* **30**, 295–405.

Prathap, G. and Babu, C. R. [1986] "An isoparametric quadratic thick curved beam element," *Int. J. Numer. Methods Eng.* **23**, 1583–1600.

Prathap, G. and Naganarayana, B. P. [1990] "Analysis of locking and stress oscillations in a general curved beam element," *Int. J. Numer. Methods Eng.* **30**, 177–200.

Raveendranath, P., Singh, G. and Pradhan, B. [1999] "A two-noded locking-free shear flexible curved beam element," *Int. J. Numer. Methods Eng.* **44**, 265–280.

Raveendranath, P., Singh, G. and Rao, G. V. [2001] "A three-noded shear-flexible curved beam element based on coupled displacement field interpolations," *Int. J. Numer. Methods Eng.* **51**, 85–101.

Ryu, H. and Sin, H. [1996] "Curved beam elements based on strain fields," *Commun. Numer. Methods Eng.* **12**, 767–773.

Saleeb, A. F. and Chang, T. Y. [1987] "On the hybrid-mixed formulation of C^0 curved beam elements," *Comput. Methods Appl. Mech. Eng.* **60**, 95–121.

Shahba, A., Attarnejad, R., Jandaghi S. S. and Honarvar, G. H. [2013] "New shape functions for non-uniform curved Timoshenko beams with arbitrarily varying curvature using basic displacement functions," *Meccanica* **48**, 159–174.

Sommanawat, W. [2010] *Kriging Based Finite Element Method for Material Discontinuities and Multiscale Simulation*, Doctoral Dissertation, Asian Institute of Technology, Pathumthani, Thailand.

Song, J. H., Wang, H. and Belytschko, T. [2008] "A comparative study on finite element methods for dynamic fracture," *Comput. Mech.* **42**, 239–250.

Stolarski, H. and Belytschko, T. [1982] "Membrane locking and reduced integration for curved elements," *J. Appl. Mech. Trans. ASME* **49**, 172–176.

Stolarski, H. and Belytschko, T. [1983] "Shear and membrane locking in curved C^0 elements," *Comput. Methods Appl. Mech. Eng.* **41**, 279–296.

Tufekci, E., Eroglu, U. and Aya, S. A. [2017] "A new two-noded curved beam finite element formulation based on exact solution," *Eng. Comput.* **33**, 261–273.

F. T. Wong & J. Gunawan

Wackernagel, H. [2003] *Multivariate Geostatistics*, 3rd Edition (Springer, Berlin).

Wang, D. and Chen, J. S. [2006] "A locking-free meshfree curved beam formulation with the stabilized conforming nodal integration," *Comput. Mech.* **39**, 83–90.

Wei, G., Lardeur, P. and Druesne, F. [2022] "A new solid-beam approach based on first or higher-order beam theories for finite element analysis of thin to thick structures," *Finite Elem. Anal. Des.* **200**, 103655.

Wong, F. T., Christabel, Y., Pudjisuryadi, P. and Kanok-Nukulchai, W. [2015] "Testing of the Kriging-based finite element to shell structures with varying thickness," *Proc. Eng.* **125**, 843–849.

Wong, F. T. and Kanok-Nukulchai, W. [2006] "Kriging-based finite element method for analyses of Reissner-Mindlin plates," *Emerging Trends*: *Keynote Lectures and Symposia—Proc. 10th East-Asia Pacific Conf. Struct. Eng. Const.*, Asian Institute of Technology, Bangkok, pp. 509–514.

Wong, F. T. and Kanok-Nukulchai, W. [2009a] "On the convergence of the Kriging-based finite element method," *Int. J. Comput. Methods* **6**, 93–118.

Wong, F. T. and Kanok-Nukulchai, W. [2009b] "Kriging-based finite element method: Element-by-element Kriging interpolation," *Civ. Eng. Dimens.* **11**, 15–22.

Wong, F. T., Santoso, S. W. and Sutrisno, M. [2022] "Locking-free Kriging-based Timoshenko beam elements using an improved implementation of the discrete shear gap technique," *Civ. Eng. Dimens.* **24**, 11–18.

Wong, F. T. and Sugianto, S. [2017] "Study of the discrete shear gap technique in Timoshenko beam elements," *Civ. Eng. Dimens.* **19**, 54–62.

Wong, F. T., Sulistio, A. and Syamsoeyadi, H. [2018] "Kriging-based Timoshenko beam elements with the discrete shear gap technique," *Int. J. Comput. Methods* **15**, 1850064-1–1850064-27.

Wong, F. T. and Syamsoeyadi, H. [2011] "Kriging-based Timoshenko beam element for static and free vibration analyses," *Civ. Eng. Dimens.* **13**, 42–49.

Wong, F. T., Tanoyo, N. and Gosaria, T. C. [2024] "Free vibration and buckling analyses of beams using Kriging-based Timoshenko beam elements with the discrete shear gap technique," *Civ. Eng. Dimens.* **26**, 21–31.

Yang, S. W., Budarapu, P. R., Mahapatra, D. R., Bordas, S., Zi, G. S. and Rabczuk, T. [2015] "A meshless adaptive multiscale method for fracture," *Comput. Mater. Sci.* **96**, 382–395.

Yang, Z., Chen, X., He, Y., He, Z. and Zhang, J. [2014] "The analysis of curved beam using B-spline wavelet on interval finite element method," *Shock Vib.* **2014**, 738162, https://doi.org/10.1155/2014/738162.

Zhang, Z. [1992] "A note on the hybrid-mixed C^{0}curved beam elements," *Comput. Methods Appl. Mech. Eng.* **95**, 243–252.